HEALTH AND MEDICINE

Programmable engineered bacteria as sustained-releasing antibody factory in situ for enhancing tumor immune checkpoint therapy

Xiao-Ting Xie[1]†, Meng Guan[1]†, Kai Cheng[1]†, Yong Li[1], Bin Zhang[1], Yi-Tong Zhou[1], Lin-Fang Tan[1], Peng-Shuo Dong[1], Si Chen[2], Bo Liu[1]*, Yuan-Di Zhao[1,3]*, Jin-Xuan Fan[1]*

Copyright © 2025 The Authors, some rights reserved; exclusive licensee American Association for the Advancement of Science. No claim to original U.S. Government Works. Distributed under a Creative Commons Attribution NonCommercial License 4.0 (CC BY-NC).

Tumor immune checkpoint therapy (ICT) aims to block immune escape signals between tumor and immune cells. However, low delivery efficiency of immune checkpoint inhibitors (ICIs), narrow single-target approach, and reduced responsiveness notably hinder clinical development of ICT. Here, we developed a nanoliposome-bacteria hybrid system that acts as an antibody (Ab) factory, enabling precise tumor targeting and macrophage activation in hypoxic environments. We reprogrammed attenuated *Escherichia coli* MG1655 to synthesize CD47 antibodies (aCD47) in response to hypoxic tumor microenvironments while surface conjugating with redox-responsive macrophage colony-stimulating factor-loaded liposomes. This system leverages bacterial tropism to enhance macrophage infiltration and polarization. The low oxygen levels trigger in situ aCD47 expression, blocking the "do not eat me" signal and boosting macrophage antitumor activity. In addition, macrophage antigen presentation activates CD8+CD3+ T cells, amplifying systemic antitumor immunity. Analysis of the gut microbiome shows reduced pathogenicity and improved intestinal tolerance with increased probiotics.

INTRODUCTION

Tumor immune checkpoint therapy (ICT) has made remarkable progress in the past decade by interfering with critical signal exchanges between tumor cells and immune cells to enhance antitumor immune responses (*1*, *2*). ICT at this stage focuses on activating adaptive immune mechanisms represented by T lymphocytes. However, the complex tumor immune microenvironment, impaired specific antigen screening, and T lymphocyte exhaustion lead to severe limitations in activity and targeting (*3*–*5*). The innate immune system represented by macrophages, with rapid immune response, wide range of antitumor targets, and relatively independent antigen-presenting ability, is gradually becoming the focus of next-generation immunotherapy and the mediator of anticancer treatments (*6*). The regulation of phagocytosis of tumor cells by macrophages is critically dependent on the fine balance between "eat me" and "do not eat me" signals on the surface of tumor cells (*7*). Also, CD47-SIRPα signaling pathway, as a classical "do not eat me" signal, has a regulatory role in this process (*8*). Unfortunately, tumor cells form immune checkpoints by up-regulating CD47 expression (three- to fivefold higher than that of normal cells), thus evading recognition and clearance by macrophages (*9*, *10*). Therefore, interfering with the interaction between CD47 on the surface of tumor cells and SIRPα on macrophages has become an effective strategy to disarm tumor immune escape and promote phagocytosis (*11*). However, the widespread expression of CD47 in all cells, anti-CD47 therapies have been limited and systemic therapy may lead to serious hemolysis problems. Also, current immune checkpoint inhibitors (ICIs), mainly monoclonal antibodies, have common limitations of protein-based drugs, including high in vivo clearance, low targeting accuracy, difficulty in maintaining local concentration, and high cost (*12*), thus hindering macrophage-based ICT.

Rapid development of synthetic biology technologies enables the use of engineered bacteria as an efficient and scalable biomanufacturing platform to produce protein-based ICIs (*13*–*15*). Meanwhile, the unique tumor microenvironment (TME) of solid tumors is characterized by hypoxia, eutrophication, and immune suppression, which is very suitable for most anaerobic and facultative anaerobic bacteria to enrich and colonize in the tumor site (*16*–*18*). The natural tendency of bacteria to the TME brings unique advantages for engineered bacteria to be used directly as innovative carriers for delivering immunotherapeutic drugs, overcoming the inherent limitations of traditional protein-based ICI delivery. Engineered bacteria are designed to carry reprogrammed genetic modules, including genetic control elements with the ability to sense and respond to specific signals with genetic circuits encoding therapeutic proteins (*19*–*21*). Precise and efficient spatiotemporal regulation enables efficient expression of ICIs in the tumor in situ, ensuring precise delivery of therapeutic agents and maximizing efficacy. Current genetic engineering strategies have enabled programmable engineered bacteria to respond to bacterial population sensing signals or external physical or chemical stimuli (isopropyl-β-d-thiogalactopyranoside, temperature, ultrasound, etc.) (*22*–*25*), but synthetic biology initiation of specific TME [such as hypoxia, low pH, and high glutathione (GSH) concentration]–related gene regulatory elements have not been incorporated into the design of engineered bacteria (*26*–*28*). This strategy not only enhances the regulation of therapeutic bacteria in the tumor to improve the safety and efficacy of therapy but also advances the development of ICT toward a smarter and more personalized approach.

[1]Britton Chance Center for Biomedical Photonics at Wuhan National Laboratory for Optoelectronics-Hubei Bioinformatics & Molecular Imaging Key Laboratory, Department of Biomedical Engineering, College of Life Science and Technology, Huazhong University of Science and Technology, Wuhan 430074, Hubei, P. R. China. [2]Hubei Key Laboratory of Plasma Chemistry and Advanced Materials, School of Material Science and Engineering, Wuhan Institute of Technology, Wuhan 430205, Hubei, P. R. China. [3]NMPA Research Base of Regulatory Science for Medical Devices & Institute of Regulatory Science for Medical Devices, Huazhong University of Science and Technology, Wuhan 430074, Hubei, P. R. China.
*Corresponding author. Email: jxfan@hust.edu.cn (J.-X.F.); zydi@mail.hust.edu.cn (Y.-D.Z.); lbyang@mail.hust.edu.cn (B.L.)
†These authors contributed equally to this work.

In this work, we address the shortcomings in the application of protein-based ICIs by designing reprogrammed engineered bacteria. Specifically, we stably transform plasmids encoding sequences for the *Escherichia coli* hypoxic promoter *fdhF* (*PfdhF*) and *pelB-CD47 antibody* (*aCD47*) into attenuated *E. coli* MG1655 to construct hypoxia response bacteria (HRB) capable of initiating the synthesis of aCD47 in a hypoxic TME (Fig. 1A). Macrophage colony-stimulating factor (M-CSF), which promotes macrophage production and activation, is also loaded into TME-responsive disulfide-containing liposomes (LMs). The LMs are covalently linked to the carboxyl groups of acetylcytidylic acid in bacterial outer membrane via amide condensation reaction, allowing LMs to be loaded on the surface of HRB to construct HRB@LM. With the specific targeting of HRB@LM to tumors, LMs are in response to the high local concentration of GSH, and a large amount of M-CSF is rapidly released to promote a large number of macrophages to infiltrate tumor. Meanwhile, lipopolysaccharide (LPS) of *E. coli* outer membrane acts as an antigenic immune adjuvant to effectively polarize local macrophages from M0 phenotype to M1 phenotype with phagocytosis ability. HRB proliferates in the tumor and initiates synthesis of aCD47 in a hypoxic TME, which competitively inhibit the "do not eat me" signal between macrophages and tumor cells and promote tumor cell killed by macrophages. The antigen-presenting ability of macrophages is significantly enhanced, which, in turn, prompt the lymphatic activation of more CD8+CD3+ T cells in vivo, effectively inhibiting distal tumor metastasis. In addition, HRB@LM is effective in reducing pathogenicity and improving intestinal tolerance, with the restoration of the gut microbiota through modulation of *Lactobacillaceae*, *Streptococcaceae*, and *Gemellaceae* abundances. In vitro and in vivo experiments demonstrate that this nanoliposome-bacteria hybridization system can precisely target tumor tissues, show smart synthesis of ICI, maintain spatiotemporal balance of macrophage activation and exhaustion, inhibit immune evasion mechanism, and regulate gut microbiota ecology. The reprogramming and redecoration of bacteria form a smart, sustainable smart antibody (Ab) factory that offers a previously unidentified approach to precision medicine related to ICT.

RESULTS

Hypoxia-responsive and tropism of HRB@LM

To investigate the role of CD47/SIRPα in different tumors, *CD47* gene derived from The Cancer Genome Atlas (TCGA) database were analyzed. Data analysis showed that immune escape–associated CD47 gene was highly expressed in patients with colon adenocarcinoma (COAD) (Fig. 1B) compared to six types of tumors [adrenocortical carcinoma (ACC), pheochromocytoma and paraganglioma (PCPG), thymoma (THYM), kidney papillary cell carcinoma (KIRP), lower grade glioma (LGG), and diffuse large B-cell lymphoma (DLBC)]. Also, in the comparison of samples from patients with COAD ($n = 275$) and healthy population ($n = 34$), it was found that *CD47* expression was significantly higher in patients with COAD (Fig. 1C). The expression of *CD47* did not fluctuate significantly in the early, middle, and late stages of COAD (fig. S1A). Therefore, a prokaryotic expression plasmid containing a hypoxia-driven therapeutic circuit applied to COAD treatment was constructed, which carries the *aCD47* gene containing the N-terminal *pelB* secretion signaling peptide and an independent tracer mCherry gene under the *PfdhF-P* tandem promoter. Subsequently, the HRB were prepared by a heat shock method. To validate the hypoxic logic circuit of HRB, the expression of mCherry and aCD47 was monitored under different incubation conditions. The result of SDS–polyacrylamide gel electrophoresis (PAGE) showed that aCD47 was significantly increased in HRB lysate and supernatant under hypoxic conditions, whereas it was almost undetectable under normoxic conditions; at the same time, both under normoxic and hypoxic conditions, HRB stably expressed the mCherry (Fig. 1D). By real-time visualization recording and fluorescence imaging, the corresponding fluorescence intensity were seen to increase significantly with time when HRB was incubated at 37°C under hypoxic conditions for 24 hours (Fig. 1E and fig. S1B). The above phenomena proved the feasibility and validity of designed sequences. To further investigate the expression and affinity of aCD47, we analyzed HRB under different oxygen concentration environments by flow cytometry. Flow cytometry analysis showed that, compared with MG1655, HRB exhibited green fluorescence signals under both normoxic (B3) and hypoxic (B1) conditions, with the signals under hypoxic conditions being significantly stronger, which confirms that hypoxia can trigger the aCD47 expression inhibition. Meanwhile, HRB showed strong red fluorescence signal under both conditions, indicating stable expression of mCherry (Fig. 1, F to H). The aCD47 expression was deduced by enzyme-linked immunosorbent assay (ELISA). The results showed that the expression level of aCD47 increased to 43.33 pmol ml^{-1} in a time-dependent manner by hypoxic incubation up to 24 hours (Fig. 1I). Figure S1C shows that more aCD47 was released from HRB in the hypoxic environment than in the normoxic environment, and these aCD47 had high affinity for hFc-CD47. In addition, confocal microscopy images showed the same results as flow cytometry analysis, confirming the high expression of aCD47 in HRB under hypoxic conditions, further validating the controllability of the hypoxic logic circuit of HRB (Fig. 1J). Red intracellular fluorescence of RAW264.7 in the HRB group can be clearly observed in fig. S2 (A to C), indicating phagocytosis of more DiI (1,1′-dioctadecyl-3,3,3′,3′-tetramethylindocarbocyanine perchlorate)–labeled CT26. The results by flow cytometry analysis showed that HRB enhanced macrophage phagocytosis by blocking CD47 signaling by about 2.5-fold relative to the MG1655 group. The above results confirmed the effectiveness of aCD47 expressed by HRB in the presence of hypoxia as a therapeutic component. All of the above results confirmed the effectiveness of HRB-expressed aCD47 as a therapeutic component. These results indicated that the designed therapeutic logic circuit can be tightly controlled and tuned by oxygen concentration, and the expressed aCD47 was biologically active, which was important for its antitumor effect.

Preparation and characterization of HRB@LM

GSH-responsive liposomes loaded with M-CSF (LMs) were prepared by a thin-film hydration method (Fig. 2A). The hydrated particle size of LM increased from 181.67 to 213.7 nm after loading with M-CSF (Fig. 2, B and C). This is consistent with the transmission electron microscopy (TEM) image showing that the LM was homogeneous and spherical with a size of 176.31 ± 18.36 nm (Fig. 2D). The encapsulation rate and loading rate were quantitatively calculated to be 22.45 and 0.55%, respectively (Fig. 2, E and F). In addition, the GSH sensitivity of LM plays a key role in triggering the release of M-CSF from the TME with high concentrations of GSH (10 μM). To investigate the response of LM to different concentrations of GSH, the size of LM was monitored. After incubation in

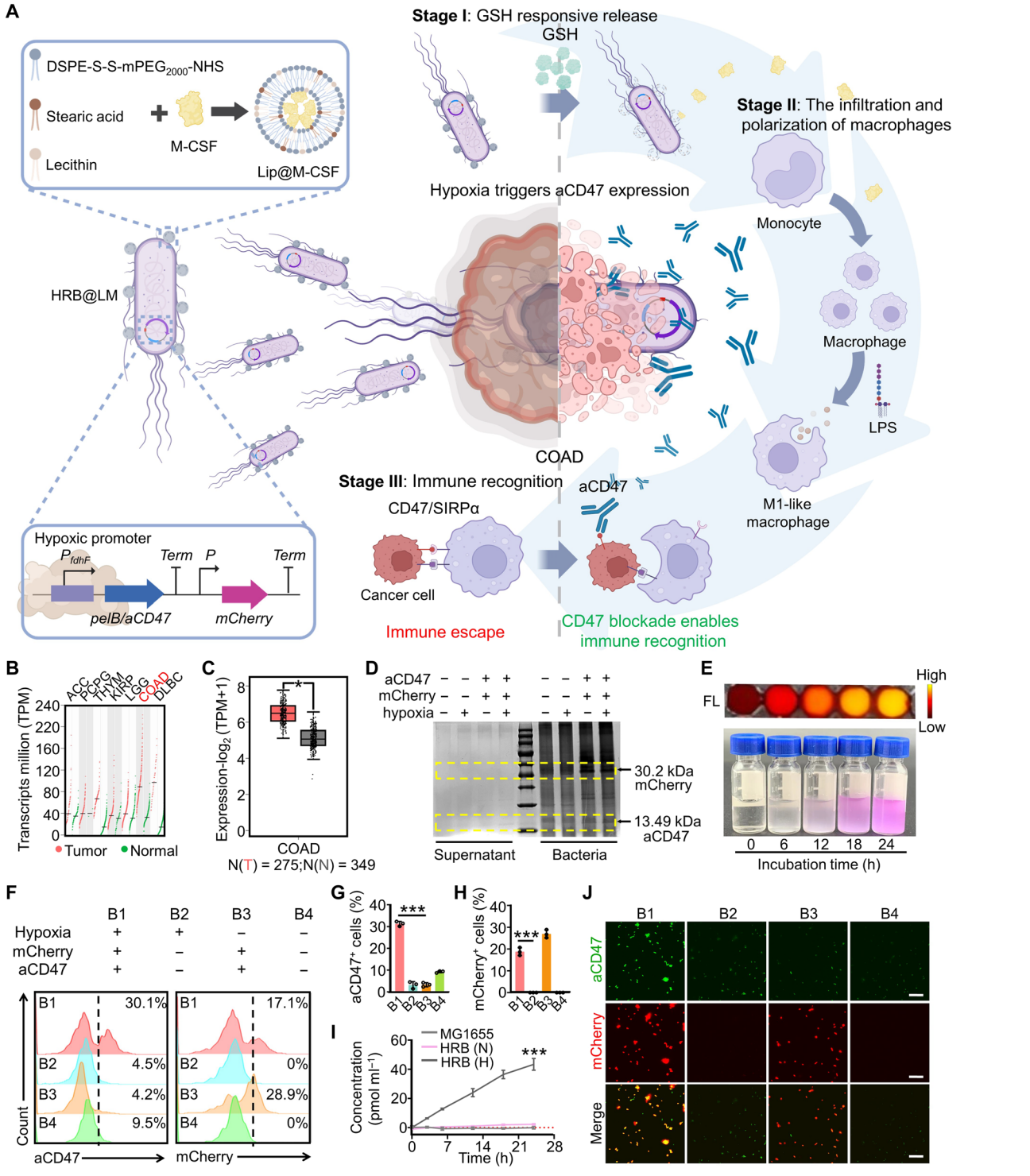

Fig. 1. Design of HRB@LM for cancer immunotherapy. (**A**) Schematic diagram of HRB@LM in controlling aCD47 expression by hypoxia invitation and the mechanism for cancer immunotherapy. (**B**) Dot plot about tissue-wise expression of CD47 in different cancer types. (**C**) Box plot about tissue-wise expression of CD47 in COAD. (**D**) Representative SDS-PAGE image of aCD47 and mCherry protein expressed in HRB. Images were representative of three experiments. (**E**) In vitro photos and fluorescence images of mCherry protein of HRB under a hypoxic environment. Images were representative of three experiments. h, hours. (**F** to **H**) Fluorescence intensities (F) and quantitative analysis of aCD47 (G) and mCherry (H) in the cells examined by flow cytometry. Data are presented as the means ± SD ($n = 3$). (**I**) Quantitative analysis of aCD47 protein content in culture medium (N represents normoxia, and H represents hypoxia). Data are presented as the means ± SD ($n = 3$). (**J**) Confocal microscopy images of aCD47 and mCherry protein expressed in HRB. Images were representative of three experiments. Scale bars, 20 μm. Significance between each of the multiple groups in (G), (H), and (I) was calculated using one-way ANOVA. (A) Created with BioRender.

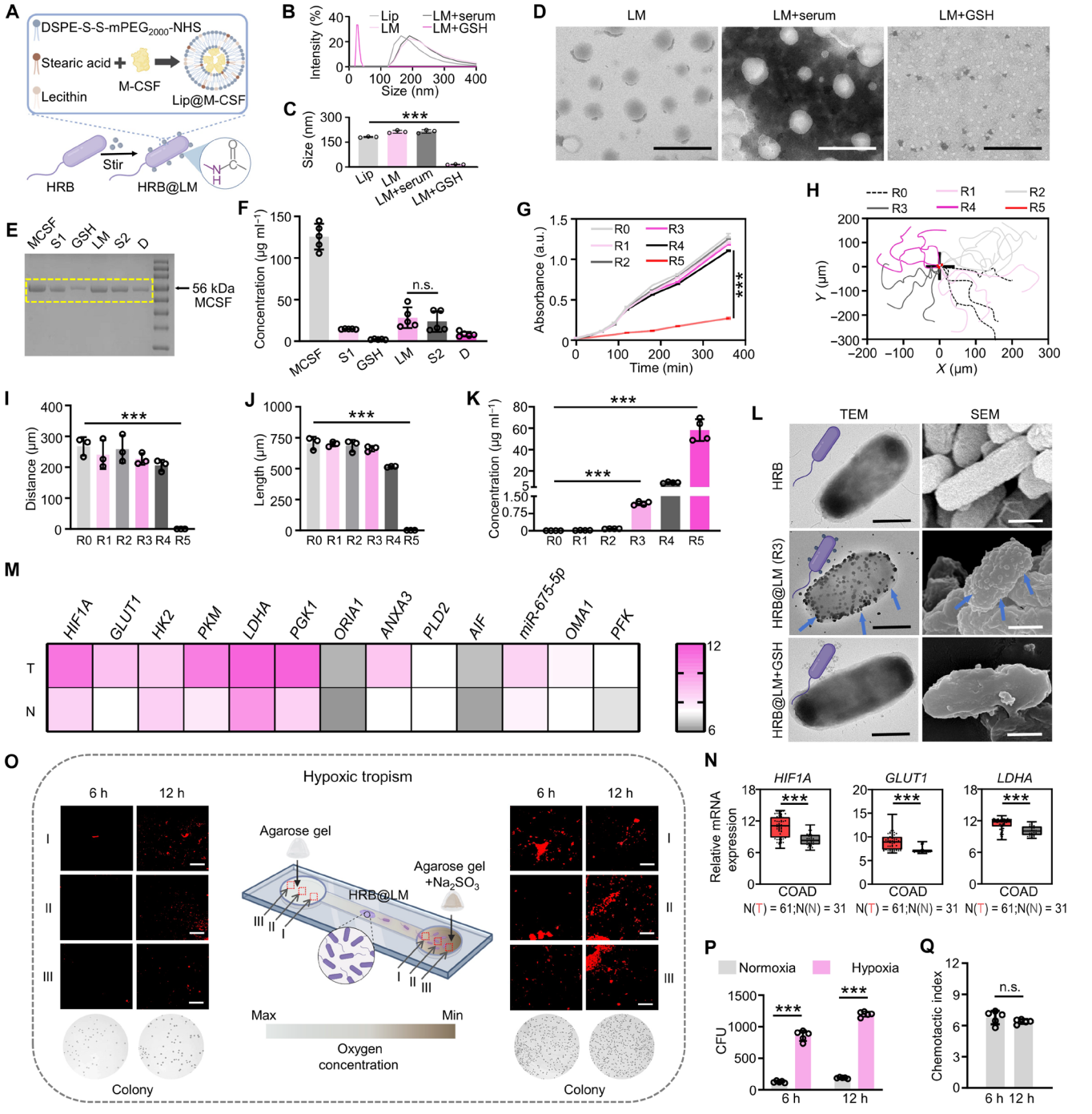

Fig. 2. Preparation and characterization of HRB@LM. (**A**) Schematic diagram of HRB@LM preparation process. (**B** and **C**) Size distribution by intensity (B) and hydrated particle sizes (C) of Lip, LM, LM+serum, and LM+GSH. Data are presented as the means ± SD ($n = 3$). (**D**) TEM images of LM and LM+GSH. (**E** and **F**) Representative SDS-PAGE image (E) and protein concentration (F) of M-CSF, S1, GSH, LM, S2, and D. M-CSF represents total synthesis solution, S1 represents the solution after removal of LM by ultrafiltration centrifugation, GSH represents the GSH solution added during response release, S2 represents the solution obtained by ultrafiltration centrifugation after response release, and D represents the filtered sample recovered by ultrafiltration centrifugation after response release. Data are presented as the means ± SD ($n = 3$). (**G**) Growth curves of R0, R1, R2, R3, R4, and R5. Data are presented as the means ± SD ($n = 3$). a.u., arbitrary units. (**H**) Movement trajectories in liquid medium. (**I** and **J**) Distance (I) and length (J) of R0, R1, R2, R3, R4, and R5. Data are presented as the means ± SD ($n = 3$). (**K**) Concentration of M-CSF in R0, R1, R2, R3, R4, and R5. Data are presented as the means ± SD ($n = 3$). (**L**) TEM images of HRB, HRB@LM, and HRB@LM+GSH. (**M**) Heatmap derived from the GSE73360 dataset. (**N**) *HIF1A*, *GLUT1*, and *LDHA* gene expression of colorectal cancers from GSE73360. (**O**) Schematic diagram, confocal images, and photos of HRB@LM in a chamber with lower oxygen concentrations. Images were representative of three experiments. (**P**) Distribution of HRB@LM in chambers. Data are presented as the means ± SD ($n = 5$). (**Q**) CI of HRB@LM. Data are presented as the means ± SD ($n = 5$). Significance between two groups in (N), (P), and (Q) was assessed by unpaired two-tailed Student's *t* test, and between each of the multiple groups in (C), (F), (G), (I), (J), and (K) was calculated using one-way ANOVA. (A and O) Created with BioRender.

mouse serum for 12 hours, the size distribution of LM was homogeneous and maintained at 215.2 nm. TEM images also showed that LM maintained a monodisperse spherical morphology. It was suggested that GSH in serum was not sufficient to trigger the release of loaded M-CSF from LM. In contrast, simulated TME with a GSH concentration of 10 μM triggered the complete deconstruction of LM to release M-CSF, and a release rate of 75.91% was calculated.

To ensure the maximum M-CSF loading in the case of bacterial proliferation, motility, and hypoxic tendency, we optimized the synthesis ratios of HRB@LM (R0, R1, R2, R3, R4, and R5) and monitored the growth curves and the trajectories (*29*). The growth of HRB was severely affected under the R5 ratio, whereas the growth of HRB was maintained well under the R1, R2, R3, and R4 ratios (Fig. 2G). Subsequently, the distance and length of the trajectories of each group were recorded and analyzed. It exhibited a low loaded M-CSF concentration in the R1 and R2 groups and impaired exercise capacity in the R4 and R5 groups. However, there was no significant change in the distance and length of trajectories of the R3 group in comparison to the HRB (Fig. 2, H to J). Also, the R3 group was able to load 1195.83 μg ml^{-1} [10^7 colony-forming units (CFU) ml^{-1}] of M-CSF after quantification via ELISA, which also ensures bacterial motility and proliferation ability (Fig. 2K). Compared with the smooth surface morphology of untreated HRB, the morphology of HRB after modified with LM revealed in Fig. 2L can be clearly observed with attached spherical particles. Also, the morphology of the HRB@LM returned to a smooth state after GSH (20 μM) treatment. The above results indicated that the optimized synthesis ratio (R3) neither interferes with the motility of HRB nor the GSH-responsive capability of LM.

Thirteen genes derived from the GSE73360 database related to hypoxia either directly (*HIF1A*) or indirectly (tumor glycolysis, invasion, metastasis, angiogenesis, and proliferation) were analyzed (Fig. 2M), and both the characteristic tumor glycolysis and the significant elevation of *HIF1A* confirmed that COAD had the distinctive feature of a hypoxic TME (Fig. 2N) (*30*–*32*). HRB@LM targeting of the hypoxic TME was an important point for precision therapy. To further evaluate whether HRB@LM inherited the natural hypoxia tropism of bacteria, the motility of HRB@LM was investigated in a microfluidic device with an oxygen concentration gradient (*33*). A total of 10^5 CFU of HRB@LM was injected into the center of channel, and three positions were taken along the direction of channel to monitor the distribution of HRB@LM (Fig. 2O). After incubation for 6 hours, the red fluorescence of mCherry could be clearly observed in the hypoxic chamber. The red fluorescence in the hypoxic chamber was gradually enhanced until 12 hours of incubation. By counting the bacteria in the chamber by the dilution coating plate method, consistent results were observed, showing that the number of recruited HRB@LM in the hypoxic chamber was much higher than that in the normoxic chamber (Fig. 2P). Also, there was no significant change between the chemotaxis indexes in 6 and 12 hours, indicating that the hypoxia tropism of HRB@LM was not affected for a short period of time (Fig. 2Q). Thus, an optimized ratio of R3 with good bacterial proliferation, motility, and anaerobic tropism was selected for subsequent experiments.

Moreover, we quantified the concentration of secreted CD47 antibody by ELISA, and the results showed that the expression level of aCD47 increased to 50.192 pmol ml^{-1} after 24 hours of hypoxic incubation in the HRB@LM group. This was not significantly different from the expression of the HRB group in the hypoxic environment (fig. S2D). Thus, LM conjugation did not affect the hypoxia-initiated expression of aCD47 for HRB.

Tumor targeting and penetrating capacity of HRB@LM

To assess the tumor targeting and penetration ability of HRB@LM, the distribution in the three-dimensional (3D) CT26 sphere model was further tested and evaluated. There was progressively stronger mCherry fluorescence observed in the center of the model sphere of HRB and HRB@LM groups (Fig. 3A). Fluorescence intensity analysis was performed after 3D construction, and spatial visualization also confirmed the deep penetration of HRB with HRB@LM into the tumor spheroids (Fig. 3B). It was addressed that the nanoliposome-bacteria hybridization system, unlike the single penetration ability of nanomaterials, inherited the nature hypoxic tropism originating from the bacteria and actively drove toward the center of the hypoxic tumor spheres. Notably, the radial fluorescence intensity of the tumor spheres was analyzed, and the fluorescence intensity of the center in the HRB group was higher than that in the HRB@LM group, indicating that the loading of the LM potentially effected on the motility of the HRB in the CT26 sphere model but does not affect their hypoxia tropism (Fig. 3, C and D).

Neutrophils are the host's first line of defense against pathogen. To explore the ability of HRB@LM to evade recognition and uptake, HRB or HRB@LM was incubated with neutrophils (*34*). It was found that HRB@LM was more capable of evading recognition by neutrophils, whereas HRB was easily cleared by neutrophil uptake (Fig. 3E). 21.3% of neutrophils uptaken with bacteria was detected in the HRB group, which was higher than 2.54% in the HRB@LM group. It was demonstrated that the load of LM contributed to the avoidance of neutrophil recognition and clearance in vivo for HRB (Fig. 3, F and G).

Subsequently, we intravenously injected 10^7 CFU of Cy5.5-labeled HRB@LM into mice, and then in vivo distribution imaging and various organ and tumor collections were investigated at 0, 3, 6, 12, and 24 hours postinjection (*35*). As shown in Fig. 3H and fig. S3A, HRB and HRB@LM with significant red fluorescence were observed at the tumor site, whereas the Cy5.5 and InBac (inactivated HRB) had no target ability. Although HRB arrived at the tumor site earlier, fluorescence intensity and residence time were not as strong as that of HRB@LM. Fluorescence signals in various organs and tumors of mice were analyzed after 24 hours of drug administration. The results showed that, although HRB partially targeted the tumor, HRB was mainly distributed in the liver and kidney. Also, HRB@LM was more enriched in the tumor site compared to the HRB group, although part of HRB@LM was distributed in the kidney (Fig. 3I and fig. S3B). TEM images of tumor tissues similarly showed a less amount of HRB in tumor tissues than HRB@LM (Fig. 3J). By imaging the maximum cross section of the tumor 6 and 24 hours after injection of HRB@LM, it was observed that a large amount of HRB@LM was distributed in the necrotic, empty areas of the tumor (Fig. 3K and fig. S3C). Various organs and tumors were collected, homogenized, and serially diluted (10 to 10,000x) for coating (*36*). The colony count on each plate showed a significant decrease in the number of colonies in the liver and kidney of the HRB@LM group as compared to the liver and kidney of the HRB group. Also, a gradual increase in colony counts over time was clearly observed in the tumor of the HRB@LM group (fig. S3, D to H). To further evaluate the penetration ability of HRB@LM at the tumor site, we sampled the tumors with a 1-mm section interval in 12 hours after injection

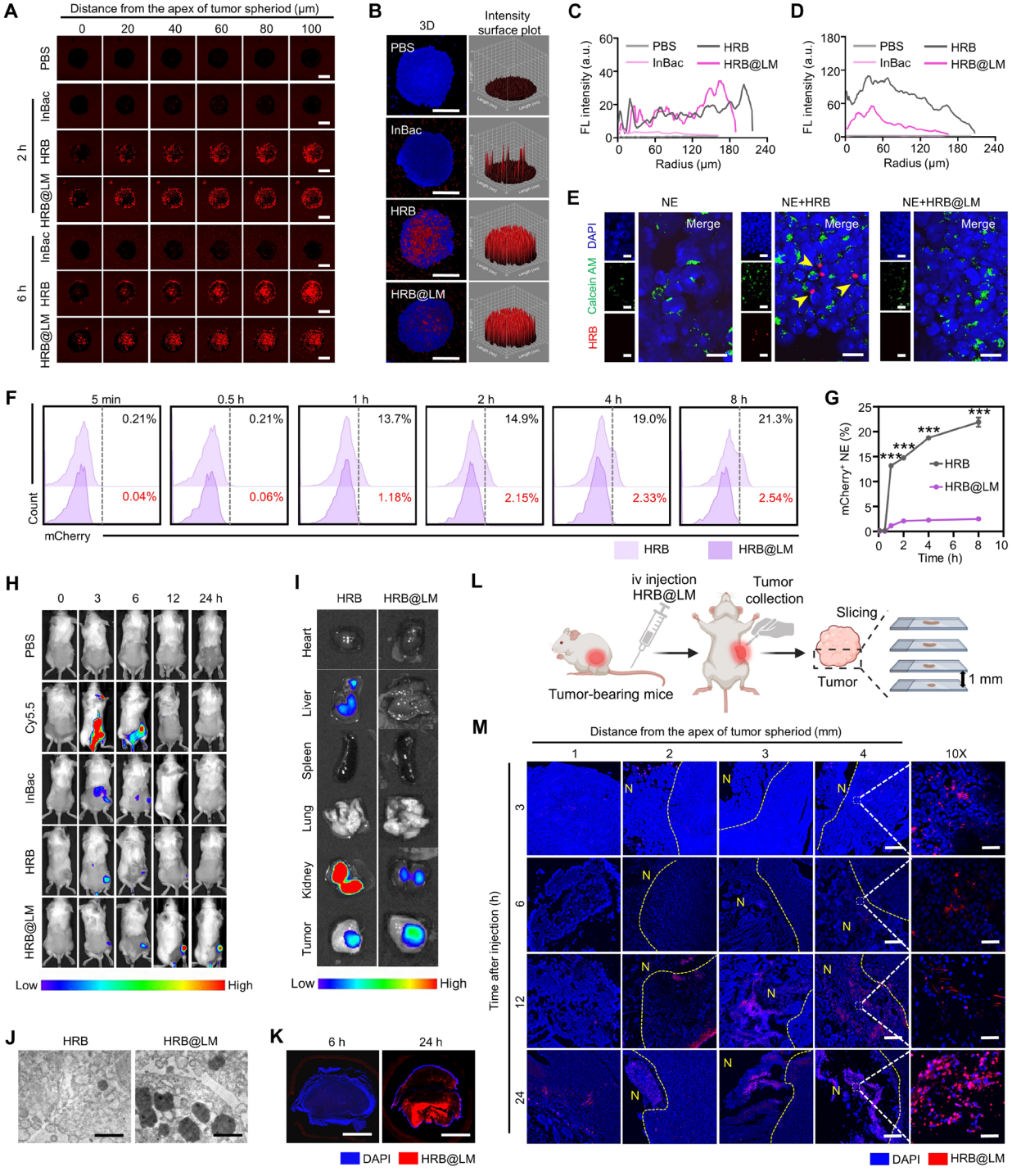

Fig. 3. HRB@LM tumor targeting and penetrating capacity. (**A**) Penetration of HRB@LM and HRB in CT26 multicellular spheroids. Images were representative of three experiments. (**B**) 3D construction and intensity surface plot of confocal images for the penetration about InBac, HRB, and HRB@LM in CT26 multicellular spheroids after 6 hours of incubation. (**C** and **D**) Quantitative analysis of fluorescence after HRB@LM and HRB incubated with CT26 multicellular spheroids for 2 hours (C) and 6 hours (D). (**E**) Fluorescence images of neutrophils (NE), NE+HRB, and NE+HRB@LM. Yellow arrows indicate the intracellular HRB@LM. Scale bars, 20 μm. Images were representative of three experiments. (**F** and **G**) Representative flow cytometry (F) and quantitative analysis (G) of HRB and HRB@LM in different cells. Data are presented as the means ± SD ($n = 3$). (**H**) Fluorescence images of mice with different treatments. Images were representative of three experiments. (**I**) Fluorescence images of major organs of mice. Images were representative of three experiments. (**J**) Representative portion of a resin-embedded section reprocessed for TEM. Scale bars, 2 μm. (**K**) Fluorescence images of the distribution of HRB@LM within tumors. Scale bars, 4 mm. Images were representative of three experiments. (**L**) Schematic illustration of tumor targeting capacity studies on colon tumor-bearing mice. iv, intravenous. (**M**) Fluorescence images about the distribution of HRB@LM in the tumor. Scale bars, 100 μm. Images were representative of three experiments. Significance between two groups in (G) was assessed by unpaired two-tailed Student's *t* test. (l) Created with BioRender.

(Fig. 3L). As shown in Fig. 3M, it can be clearly observed that the Cy5.5-labeled HRB@LM gradually migrated to the necrotic region of tumor with time. By fluorescence colocalization of HIF1A and bacteria within the tumor, the location of enhanced green fluorescence (HIF1A) accompanied by aggregated red fluorescence (HRB@LM) can be clearly observed in fig. S3I. The above results suggest that the distribution of bacteria in vivo is hypoxia tropic and thus targeted to tumors with hypoxic properties. Overall, these results were attributed to biochemically unique TME, providing strong evidence for HRB@LM evasion of in vivo clearance and targeted colonization of hypoxic and necrotic areas.

HRB@LM mediates macrophage activation and "CD47-SIRPα" signal blocking

To evaluate the recruitment of macrophages, we inoculated HRB@LM in the lower chamber of the transwell, and macrophages were cultured in the upper chamber. The effect of recruitment in the different groups was analyzed by counting the number of macrophages migrating to the lower chamber after 24 hours (Fig. 4A and fig. S4A). As expected, the crystal violet staining results exhibited that the number of macrophages recruited by HRB and HRB@LM+GSH was significantly higher than the number of macrophages recruited by the phosphate-buffered saline (PBS), InBac, and HRB@LM groups (Fig. 4B). This indicated that HRB@LM had the same ability to recruit macrophages as HRB in response to GSH. In addition, the number of macrophages in the HRB@LM+GSH group was greater than that in the HRB group, which could be attributed to the regulation of macrophage proliferative capacity by M-CSF. Subsequently, the phenotype of macrophages recruited in the HRB@LM group was investigated by flow cytometry. The CD86+ cell ratio in the HRB@LM+GSH group showed 3.9-fold of that in the PBS group. Also, there was no significant difference between the CD86+ cell ratio in the M-CSF group and that in the PBS group (Fig. 4C and fig. S4B). These suggested that the macrophages recruited from the HRB@LM+GSH group exhibit an inflammatory phenotype. Compared with the HRB (supernatant) group, aCD47 combined with bacteria promoted macrophage polarization to enhance phagocytosis about eightfold in the HRB group. The results indicated that therapeutic efficacy of aCD47 enhanced with macrophage repolarization. To further verify that the "do not eat me" signal was blocked in the HRB@LM+GSH group, DiI-labeled CT26 cells were incubated in the lower chamber of transwell for 24 hours. Figure 4D shows that HRB@LM+GSH-treated macrophages exhibited abundant pseudopods and omelette structures with more red fluorescence. Also, the flow cytometry analysis showed that the ratio of DiI+ cells increased, which indicated that HRB@LM+GSH could effectively block the "do not-eat me" signal and promote the phagocytosis of tumor cells by macrophages.

To assess the penetration ability of HRB@LM-recruited macrophages within the tumor, Calcein AM–labeled RAW264.7 was added to 3D CT26 tumor spheroids coincubated with HRB@LM or HRB for 2 hours in advance. After 6 hours of incubation, macrophages migrating into the tumor spheroids of HRB@LM and HRB groups were clearly observed. However, fluorescence intensity analysis was performed by 3D reconstruction of the confocal fluorescence images, and spatial visualization was used to discern the depth of penetration of macrophage into the tumor spheroids (Fig. 4, E to H). The results showed that more macrophages penetrated a deeper part of tumor spheroids in the HRB@LM group compared to the HRB group, which might be attributed to the loading of LM fueling HRB to evade macrophage activation and clearance outside tumor spheroids and more HRB@LM colonizing hypoxic center recruited macrophages to infiltrate tumor spheroids. The same phenomenon we observed in vivo imaging experiments, the Cy5.5-labeled RAW264.7 fluorescence signal in tumors of mice injected with HRB in advance, was significantly different from the fluorescence in the PBS group only at 48 hours. In contrast, the fluorescence signals in tumors of mice injected with HRB@LM in advance showed significant enrichment at 36 hours and remained significantly different from the PBS group at 72 hours (Fig. 4I and fig. S4C). The above data confirmed that HRB@LM could recruit more macrophages to the tumor by evading clearance in vivo. To intuitively and visually observe HRB@LM recruiting macrophages within the tumor, we observed the location of macrophages in mouse tumors using confocal fluorescence microscopy and intravenously injected fluorescein isothiocyanate (FITC)–dextran [molecular weight (MW) = 2000 kDa] to label blood vessels. Relative to the HRB group, a large number of F4/80-labeled macrophages in the HRB@LM group infiltrated from blood vessels into tumor (Fig. 4J).

To explore whether HRB@LM triggered the same inflammatory response in normal tissues, we injected HRB@LM into paws and monitored locally associated inflammatory cells. The different groups of inflammatory cells were categorized and counted by characterizing macrophages (indicated by yellow arrows) and neutrophils (indicated by blue arrows) after hematoxylin and eosin (H&E) staining (Fig. 4, K and L). More neutrophils were present in local tissues of mice treated with InBac and HRB compared to mice treated with PBS. Also, the number of macrophages was significantly increased in the mice treated with HRB@LM+GSH. Furthermore, the phenotype of macrophages treated with HRB@LM+GSH was investigated. It was revealed that up-regulation of the expression of F4/80 (macrophage markers) and interleukin-1b (IL-1b) (inflammatory cytokine) was clearly observed in HRB@LM+GSH (Fig. 4M). In addition, the green fluorescence intensity (CD86+ cells) was significantly enhanced in the HRB@LM+GSH group relative to that in the HRB@LM group (Fig. 4, N and O). The above data suggested that HRB@LM did not trigger seriously inflammatory response in normal tissues but only recruited macrophages in response to high GSH concentrations and promotes inflammatory phenotype.

HRB@LM for in situ colon cancer treatment

To evaluate the antitumor effects of HRB@LM in vivo, in situ colon cancer mouse models were grouped and treated according to the protocol in Fig. 5A (*37*, *38*). The results of body weight monitoring showed that systemic administration of HRB@LM in five groups did not seriously affect the body weight of mice (fig. S5A). As shown in Fig. 5B and fig. S5B, similar fluorescence signals were observed in each group on day 0, indicating successful development of in situ colon cancer. After two treatments, G1 and G2 groups showed slight tumor suppression compared to the G0 group, whereas G3 and G4 groups showed relatively better tumor suppression. Further enhancement of green fluorescence signal in G3 and G4 was also detected by terminal deoxynucleotidyl transferase–mediated deoxyuridine triphosphate nick end labeling (TUNEL) assay, suggesting stronger tumor cell apoptosis relative to G0, G1, and G2 (Fig. 5C). In addition, G0, G1, G2, and G3 showed different degrees of reduction in Ki67 expression, whereas the greatest reduction in Ki67 expression was demonstrated in G4, performing a significant reduction in

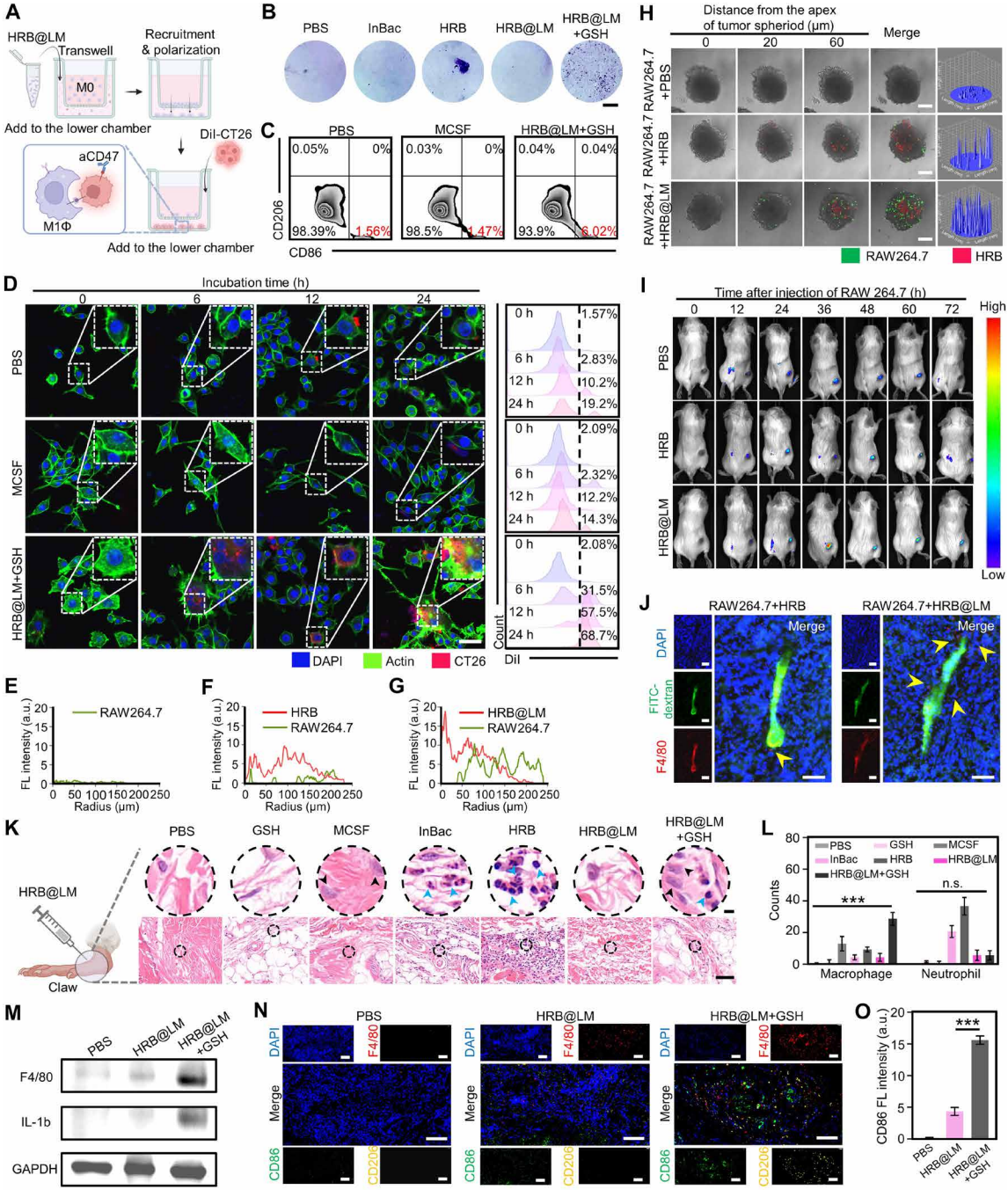

Fig. 4. Recruitment and polarization of macrophage to exhibit antitumor activity. (**A**) Schematic illustration of recruitment and polarization of macrophages in vitro to block "do not eat me" pathway. (**B**) Images of the cell recruitment assay. Scale bar, 2500 μm. Images were representative of three experiments. (**C**) Polarization analysis of RAW264.7 cells by flow cytometry. (**D**) Fluorescence images and flow cytometry analysis of polarized RAW264.7 cells phagocytic CT26 cells. Images were representative of three experiments. (**E** to **G**) Quantitative analysis of fluorescence intensity for RAW264.7+PBS (E), RAW264.7+HRB (F), and RAW264.7+HRB@LM (G) in (D). (**H**) Penetration of RAW264.7 in CT26 multicellular spheroids. The figure on the right is a 3D surface plot of RAW264.7. (**I**) Fluorescence image of the distribution of Cy5.5-labeled RAW264.7 cells in mice. Images were representative of three experiments. (**J**) Representative in vivo fluorescence images of F4/80-labeled macrophages (red) and FITC-dextran (MW = 2000 kDa)–labeled blood vessels (green) in the tumor. Yellow arrows indicate the recruitment of macrophages to tumor. Scale bars, 50 μm. Images were representative of three experiments. (**K**) H&E staining images. Scale bars, 50 μm and 2 μm (enlarged view). Black arrows mark macrophages, and blue arrows mark neutrophils. Images were representative of three experiments. (**L**) Quantification of macrophages and neutrophils numbers. Data are presented as the means ± SD ($n = 3$). (**M**) Expression of F4/80 and IL-1b in the tissue of claw detected by WB. Images were representative of three experiments. GAPDH, glyceraldehyde-3-phosphate dehydrogenase. (**N** and **O**) Representative IF images (N) and fluorescence intensity (O) of the tissue stained with F4/80 (red), CD86 (green), CD206 (yellow), and DAPI (blue). Scale bars, 100 μm. Images were representative of three experiments. Data are presented as the means ± SD ($n = 3$). Significance between each of the multiple groups in (L) and (O) was calculated using one-way ANOVA. (A and K) Created with BioRender.

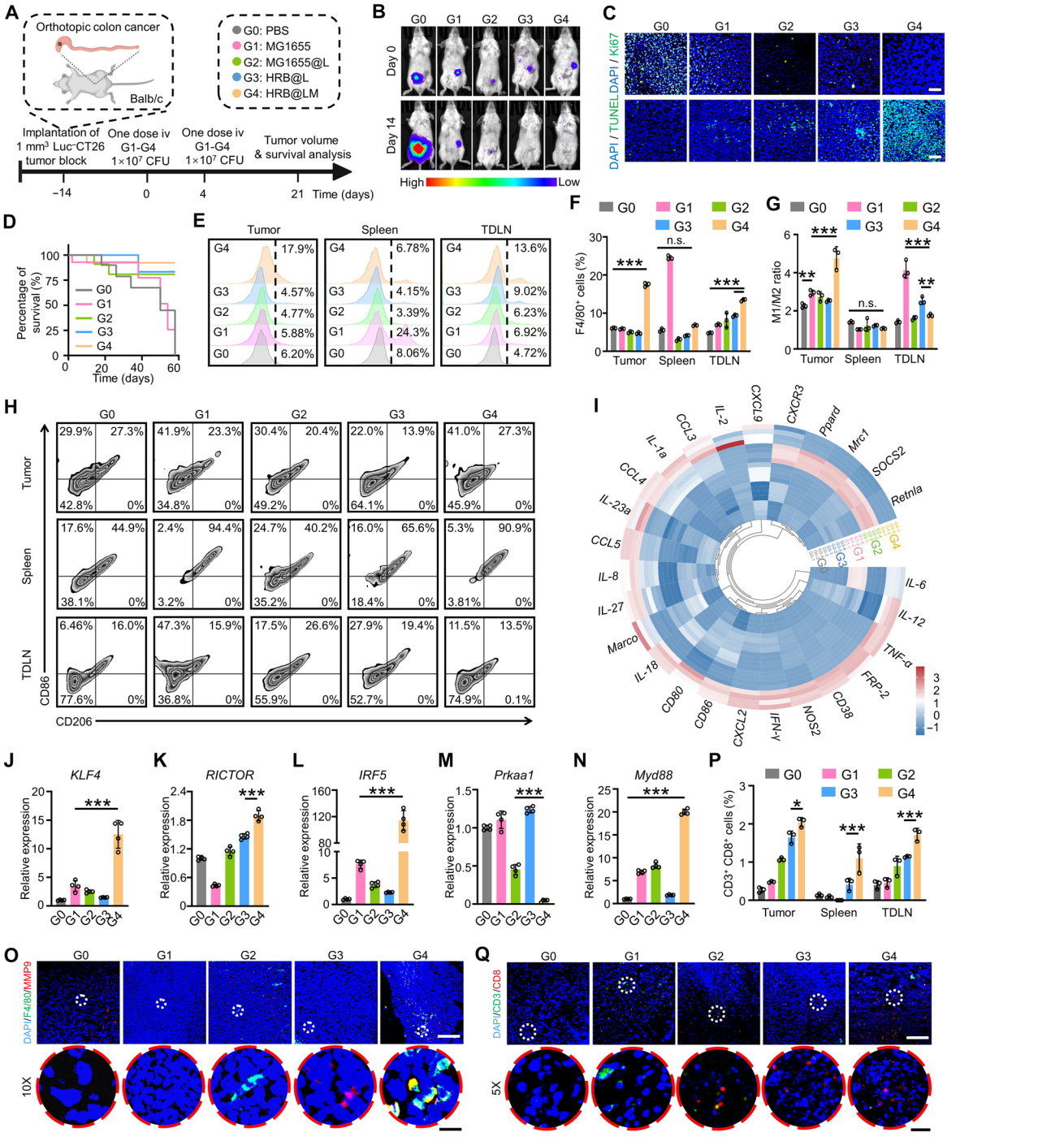

Fig. 5. HRB@LM-mediated tumor immunotherapy. (**A**) Schematic illustration of HRB@LM-mediated tumor immunotherapy in an orthotopic colon cancer mouse model. (**B**) Representative bioluminescence images of orthotopic colon cancer mice. Images were representative of three experiments. (**C**) TUNEL-stained and Ki67-stained tumor slices. Scale bars, 100 μm. Images were representative of three experiments. (**D**) Survival curves for different groups ($n = 8$). (**E** and **F**) Flow cytometry analysis (E) and quantification (F) of the percentage of F4/80+ cells. Data are presented as the means ± SD ($n = 3$). (**G** and **H**) Quantification of M1/M2 ratio (G) and flow cytometry analysis (H) of CD86+ macrophages (CD86+F4/80+) and CD206+ macrophages (CD206+F4/80+) in the tumor, TDLNs, and spleen. Data are presented as the means ± SD ($n = 3$). (**I**) Heatmap of differential gene cluster analysis of M1- and M2-related phenotypes. (**J** to **N**) Quantification of relative gene expression about macrophage polarization regulators [*KLF4* (J), *RICTOR* (K), *IRF5* (L), *Prkaa1* (M), and *Myd88* (N)]. Data are presented as the means ± SD ($n = 4$). (**O**) Images of IF staining tumor tissues [green: macrophages, red: M1-like macrophages, and blue: nuclei; scale bars, 100 μm and 10 μm (enlarged view)]. Images were representative of three experiments. (**P**) Flow cytometry quantification of CD8+ T cell (CD8+CD3+) in the tumor, TDLN, and spleen. Data are presented as the means ± SD ($n = 3$). (**Q**) Images of IF staining tumor tissues [green: T cells, red: cytotoxic T cells, and blue: nuclei; scale bars, 100 μm and 20 μm (enlarged view)]. Images were representative of three experiments. Significance between each of the multiple groups in (F), (G), (J), (K), (L), (M), (N), and (P) was calculated using one-way ANOVA. (A) Created with BioRender.

tumor proliferation. Notably, the survival time of mice in G3 and G4 was significantly prolonged compared with other groups, and the survival rates after 60 days of treatment were 83.33 and 92.85%, respectively. It was indicated that both HRB and HRB@LM exhibited good antitumor effects in in situ colon cancer (Fig. 5D). Blood routine examination and biochemical examination were operated in mice intravenously injected with HRB and HRB@LM. It was found that the relevant biochemical parameters [aspartate aminotransferase (AST), alanine amiotransferase (ALT), urea (UREA), and creatinine (CREA)] were in the normal range of values, but hematologic toxicity was unavoidable induced in the HRB group, which showed a rise in the number of neutrophils and a drop in the number of red blood cells after 24 hours postinjection (fig. S5, C and D). HRB@LM had no significant effect on these parameters, possibly due to the modification of LM to improve the safety of bacterial targeting of tumors in the circulation. In addition, H&E staining of major organs (heart, liver, spleen, lungs, and kidneys) in all five groups of mice on day 7 after injection showed no significant pathological changes and lymph node enlargement subsided after treatment (fig. S5, E and F). The above results indicated that, although HRB showed tumor growth inhibition ability in in situ colon cancer as HRB@LM, HRB@LM had lower hematological toxicity and good biological safety.

By imaging and localizing the macrophage distribution within the tumor in fig. S6A, it can be observed that macrophages in the G1 group were distributed in the periphery of the tumor tissue 24 hours after tail vein injection, whereas macrophages migrated toward the interior of the tumor tissue in the G2, G3, and G4 groups. This suggested that loaded bacteria promoted macrophage migration to the tumor core more rapidly. Subsequently, we explored whether ICT triggered by HRB@LM around macrophages activated intratumoral immune responses. Flow cytometry analysis showed that the percentage of F4/80+ macrophages in the tumor of G4 (4.788%) was significantly higher than that of other groups, suggesting that HRB@LM effectively promoted macrophage infiltration into the tumor. Also, the significant increase in F4/80+ macrophages in the tumor-draining lymph nodes (TDLNs) suggested that HRB@LM might recruit more macrophages through the TDLN (Fig. 5, E and F). The mechanism of HRB@LM-mediated ICT was investigated by in-depth phenotyping of recruited macrophages. Compared with G0, the ratio of macrophage M1/M2 (CD86+ cells/CD206+ cells) at the tumor site was significantly higher in G4, whereas the ratio of M1/M2 at the TDLN changed negligibly. In contrast, the percentage of splenic macrophages was elevated and the M1/M2 ratio in the TDLN was up-regulated in G1, and the M1/M2 ratio in the TDLN was also up-regulated in G3. These results suggested a more targeted spatiotemporal recruitment of macrophages into the tumor via the TDLN, sequential polarization to exhibit a pro-inflammatory phenotype, and consequently tumor cell killing in G4 (Fig. 5, G and H, and fig. S6B). In addition, we performed transcriptome analysis of polarization-related genes of macrophages in the tumor. As shown in Fig. 5 (I to N), compared with G0, the up-regulation of some M1-related markers [*CD80*, *CD86*, *CXCL2*, *interferon*-γ (*IFN*-γ), *NOS2*, *CD38*, *FRP2*, *tumor necrosis factor*–α (*TNF*-α), *IL-6*, *IL-8*, *IL-27*, *Marco*, *IL-18*, *CCL5*, *IL-23a*, *CCL4*, *IL-1a*, *CCL3*, *CXCL9*, and *CXCR3*] was induced in G4, whereas M2-related markers (*IL-12*, *PPARD*, *Mrc1*, *SOCS2*, and *Retnla*) showed no significant changes. In addition, polarization-associated regulators (*KLF4*, *RICTOR*, *IRF5*, *Prkaa1*, and *Myd88*) were significantly affected in G4, whereas no significant changes were observed in G3 except for the up-regulation of *IL-1a*, *CCL4*, and *IL-8* (M1-related markers). These results suggested that HRB@LM induced macrophage infiltration and M1 polarization within the tumor. This might be due to the M-CSF released in response, which stimulates monocyte differentiation and activating macrophage proliferation. Last, more macrophages infiltrate the tumor and polarize to an inflammatory phenotype in the tumor after LPS stimulation. In addition, colocalization of F4/80+MMP9+ macrophages by immunofluorescence (IF) staining on tumor tissue sections, the consistent result can be observed in Fig. 5O. A large number of M1-type macrophages could be observed infiltrating the tumor tissue in G4 compared to the rest of groups. Moreover, to investigate the aCD47 antibody expressed in tumoral hypoxic microenvironment, the distribution of aCD47 and HRB was locally imaged. As shown in fig. S6C, there was a large amount of green fluorescence (aCD47) and red fluorescence (HRB) in HRB@LM. By analyzing the radial fluorescence intensity, it could be found that, although the HRB were accompanied by a high concentration of aCD47 around the bacteria, the aCD47 was also able to diffuse into tumor tissues far away from the bacteria as compared to the MG1655 control group. Thus, aCD47, as a therapeutic component, can be anaerobically initiated to be expressed within the tumor and diffused away.

Macrophages were a class of cells with phagocytosis and antigen-presenting functions. Blockade of CD47/SIRPα-associated immune escape mechanism between macrophages and tumors can help activate T cells to enhance the role of adaptive immunity in ICT (*39*, *40*). In transcriptome analysis, it was found that IL-2 expression, which was related to adaptive immunity and can be used to activate T cells, was significantly elevated in G4, which was attributed to the initiation of immune recognition by aCD47 produced by HRB. Subsequently, in the results of flow cytometry analysis, the greatest increase in the ratio of CD8+CD3+ T cells in the tumor, spleen, and lymph of G4 was shown, as compared with the rest of the group (Fig. 5P). Also, the consistent result was found after colocalization of CD8+CD3+ T cell IF staining of tumors (Fig. 5Q and fig. S7, A to C). In conclusion, macrophages with HRB@LM treatment infiltrated tumors and enhanced adaptive antitumor immunity by blocking the "CD47/SIRPα" signal in the TME, which ultimately enhanced antitumor effect.

HRB@LM alters the gut microbiome

Next, we analyzed the changes in gut microbiome of HRB@LM-treated mice by 16*S* ribosomal RNA gene sequencing (*41*–*43*). In this study, HRB@LM was injected into normal mice by tail vein and analyzed in comparison with the structure of gut microbiota community in normal mice. As shown in fig. S8 (A to C), the Normal+HRB@LM group and Normal group exhibited a similar microbial community structure and diversity at the family level. The intestinal flora was not significantly dysbiotic after HRB@LM injection, and the diversity of phenotypic composition was not significantly changed. Unlike PBS-treated colon cancer mice, the HRB@LM-treated and Normal groups exhibited a similar microbial community structure and diversity at the family level (Fig. 6, A and B). Beta diversity analysis similarly showed that HRB@LM intervention tended to restore the gut microbial community structure altered by colon cancer (Fig. 6C). The microbial dysbiosis index (MDI) was significantly reduced in the HRB@LM group compared to that in the PBS group, but there was no significant change compared to that of the Normal group (Fig. 6D). Specifically, the relative abundance of *Lactobacillaceae* was significantly increased in the HRB@LM group compared to that in

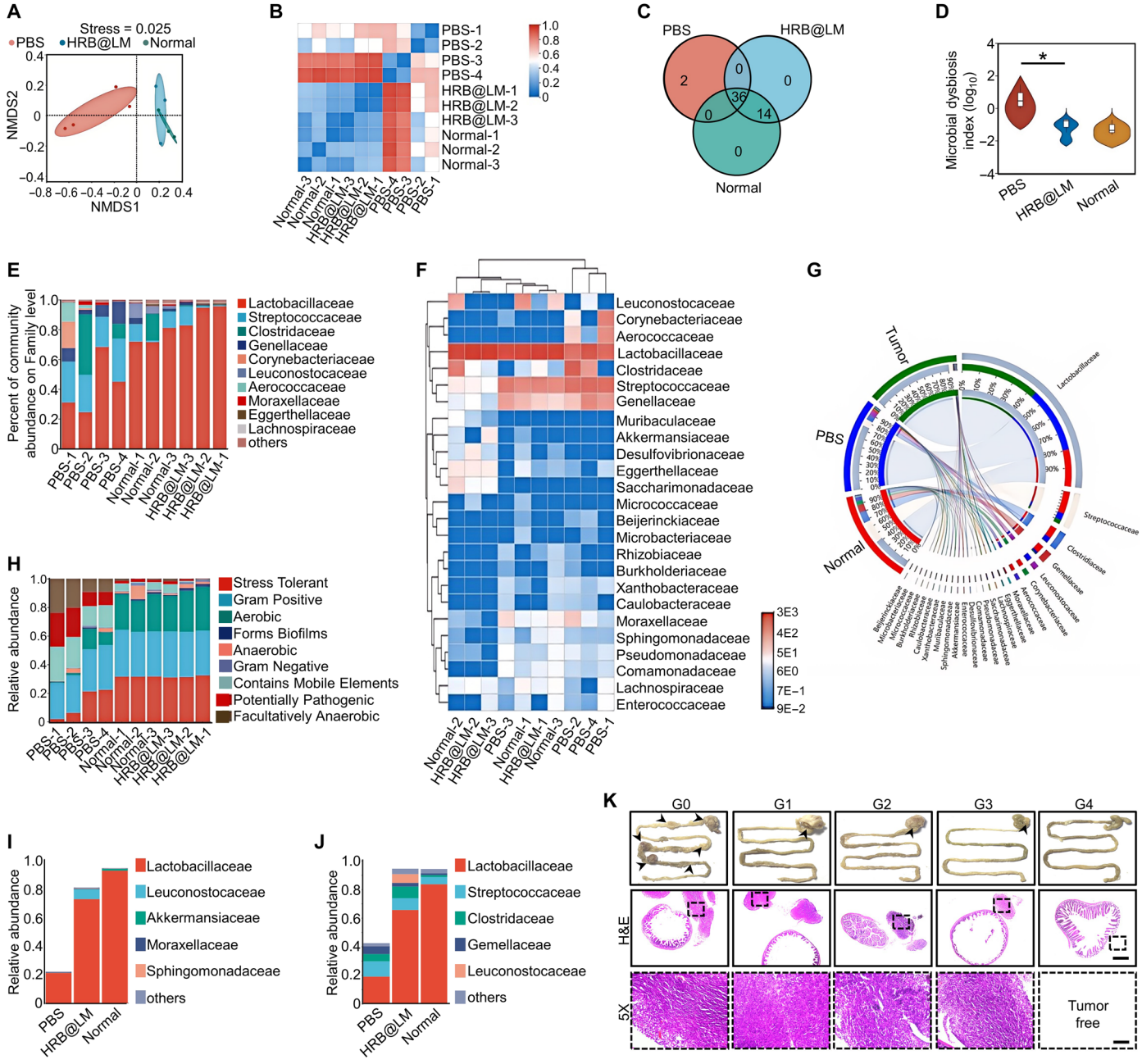

Fig. 6. Distinct gut microbial communities promoted by treatment with HRB@LM. (**A**) NMDS (nonmetric multidimensional scaling) score plot (based on Bray-Curtis). (**B**) Sample distance heatmap on the family level. (**C**) Venn diagrams to analyze the number of species shared and unique to multiple samples. (**D**) MDI of different samples. Data are presented as the means ± SD ($n = 3$). (**E**) Community bar plot analysis on the family level. (**F**) Community heatmap analysis of the family level. (**G**) Circos diagram about the relationship between samples and species. (**H**) Variation in composition of phenotype. (**I** and **J**) Community bar plot analysis of the contribution of different species to the stress tolerant (I) and aerobic (J). (**K**) Representative images and H&E of the colon tissue are shown. Images were representative of three experiments. Significance between each of the multiple groups in (D) was calculated using one-way ANOVA.

the PBS group. *Lactobacilli* have been reported to attenuate intestinal damage; enhance the intestinal immune barrier, epithelial cell barrier, and mucus barrier; and are one of the representative bacteria involved in adjuvant therapy for inflammatory bowel disease and colon cancer (*44*, *45*). Moreover, the relative abundances of pathogenic *Streptococcus* and *Gemellaceae* were reduced in the HRB@LM group, which were strongly associated with the development and progression of colon cancer (Fig. 6, E and F) (*20*, *46*, *47*). Circos plots more visually showed the relative abundance of each intestinal bacterial family category as a percentage of the total number of mice with colon cancer in both Normal and PBS groups, including *Lactobacillaceae* (75%), *Streptococcaceae* (8%), and *Gemellaceae* (2%) (Fig. 6G). Subsequent BugBase prediction-based analysis of the effects of HRB@LM treatment on gut microbial phenotypes identified nine potential microbial phenotypes, which include aerobic, anaerobic, Gram-positive, Gram-negative, biofilm-forming, pathogenic

potential, mobile element–containing, oxygen-using, and oxidative stress–tolerant phenotypes. The types of aerobic and oxidative stress tolerance were significantly increased under HRB@LM treatment, whereas the potential pathogenicity was greatly reduced (Fig. 6H). Bacterial types associated with aerobic and oxidative stress tolerance were presented, further demonstrating that HRB@LM mainly modulates *Lactobacillaceae*, *Streptococcaceae*, and *Gemellaceae* in colon cancer and thus restored the structure of the intestinal microbial community that had been altered by colon cancer (Fig. 6, I and J). By staining the intestines of five groups with H&E, it can be clearly observed that there were negligible tumor tissues in the colon of G4 compared to that of other groups and restored the normal intestinal structure (Fig. 6K). Therefore, the alteration of the bacterial community structure after HRB@LM treatment in mice with colon cancer is a result of the eradication of the tumor, leading to a subsequent change in the structure of the gut microbiota community and the formation of an environment more conducive to the growth of healthy gut microbiota community. This change in the structure of the microbial community may help to prevent recurrence of the tumor.

Inhibition of distant tumor growth and metastasis by HRB@LM

CT26 cells were subcutaneously inoculated in the right hindlimb and left hindlimb of Balb/c mice referring to the schedule shown in Fig. 7A (*20*). To investigate the effect of the treatment on the tumor foci without hypoxic core during the bacterial treatment, the distal tumors (without hypoxic cores) and the primary tumors received different treatments. Also, that HRB@LM entered more into primary tumors at the same time (fig. S9, A and B). After treatment of first inoculated CT26 tumors, there was slight tumor suppression in G1 and G2 compared with G0. Relatively better tumor suppression was found in G3 and G4 groups (fig. S9C). Also, the growth of distal subcutaneous tumors was inhibited relatively more effectively in G4 (Fig. 7, B and C). To observe the H&E sections of distal tumors in different groups, it was found that G1, G2, G3, and G4 had different degrees of tumor tissue cavitation and necrotic areas (Fig. 7D). The relatively strongest green fluorescence signal in G4 was also found via TUNEL assay, indicating that G4 treatment resulted in stronger tumor cell apoptosis. In addition, the G4 demonstrated the greatest reduction in Ki67 expression, showing a significant reduction in tumor proliferation (Fig. 7E). Colocalization of F4/80+MMP9+ inflammatory macrophages by IF staining was performed on tumor tissue sections. A large number of macrophages infiltrating the tumor tissue with M1 phenotype were observed in G4 compared to the rest of group (Fig. 7F). Infiltrating T cells in the subcutaneous tumors, TDLN, and spleen were further detected via flow cytometry. Figure 7G shows a maximal increase in the ratio of CD3+CD8+ T cells in the tumors, spleen, and TDLN in G4 relative to the rest of groups. The consistent result can be observed in the colocalization results of CD3+CD8+ T cell IF staining (Fig. 7H).

The well-adapted immunity triggered by HRB@LM and the modulation of intestinal flora encouraged us to further evaluate the efficacy of HRB@LM on tumor metastasis (Fig. 7I). No abnormal weight loss was observed in mice across treatments (fig. S9D). Notably, bioluminescence imaging of mice in G0 confirmed occurrence and proliferation of metastatic tumor cells in lung tissue (Fig. 7J). Also, the metastatic tumor nodules on the lung tissues could be clearly observed after lung tissues collected and fixed with Bouin's trichrome. Compared with the rest of group, HRB@LM (G4)–treated lungs had fewer metastatic tumor nodules, no significant increase in weight, and weak bioluminescence intensity (Fig. 7, K and L). H&E staining also confirmed that there were fewer metastatic lesions in G4 compared to the large number of metastatic lesions that appeared in lung tissues of G0, demonstrating the efficacy of the HRB@LM treatment on tumor metastasis. In addition, flow cytometry analysis and IF staining of T cells in spleens of mice were performed. It was found that the proportion of toxic T (CD3+CD8+) in the spleens of G4 was significantly elevated (Fig. 7, M and N), confirming that HRB@LM generated a long-term immune memory and successfully inhibited the occurrence of metastatic tumors.

HRB@LM for lung cancer treatment

Next, we assessed the extent of response of HRB@LM in CD47 high-expressing tumors in lung cancer. Flow cytometry analysis showed that the proportion of F4/80+ macrophages in the tumors of the G4 group was significantly higher than that of other groups (Fig. 8A), suggesting that HRB@LM effectively promoted macrophage infiltration into tumors. In addition, HRB@LM may recruit more macrophages through the TDLN, resulting in a similarly significant increase in the number of F4/80+ macrophages in the TDLN (Fig. 8B). Subsequently, we performed a detailed phenotypic analysis of the recruited macrophages. The ratio of M1/M2 macrophages (CD86+ cells/CD206+ cells) was significantly higher in the tumor and TDLN of the G4 group compared to the G0 group, whereas the ratio of macrophages in the spleen did not change significantly (Fig. 8C). Meanwhile, we performed transcription analysis of genes related to popularization of macrophages in tumors. As shown in Fig. 8D, the expression of some M1-related markers (*IFN*-γ and *TNF*-α) was up-regulated in the G4 group compared with the G0 group, whereas no significant changes were observed in M2-related markers (*IL-12* and *Retnla*). Polarization-related regulators (*KLF4* and *IRF5*) were significantly up-regulated in the G4 group. Colocalization of F4/80+MMP9+ macrophages by IF staining on tumor tissue sections, consistent results can be observed in Fig. 8E. A large number of M1-type macrophages were seen infiltrating the tumor tissue in the G4 group compared to the remaining groups. In addition, the results of flow cytometry analysis showed that there was a maximum increase in the proportion of CD8+CD3+ T cells in the tumors, spleen, and lymph nodes in the G4 group compared to the remaining groups (Fig. 8F and fig. S10, A to D). TUNEL staining tumor tissues showed enhanced green fluorescence signals in both G3 and G4 groups, which indicated that apoptosis of tumor cells was more obvious compared to G0, G1, and G2 groups (Fig. 8G). Thus, HRB@LM triggered ICT around macrophages in a mouse lung cancer model.

HRB@LM for pancreatic cancer treatment

The coexistent results were also validated in a mouse pancreatic cancer model. Flow cytometry analysis showed that the proportion of F4/80+ macrophages in the tumor, spleen, and TDLN was significantly higher in the G4 group, but macrophages in the spleen were not significantly polarized (Fig. 8, H to J). Moreover, some M1-related markers (*IFN*-γ and *TNF*-α) and polarization-associated regulators (*KLF4* and *IRF5*) were significantly up-regulated in the G4 group (Fig. 8K). A large number of M1-type macrophages infiltrating the tumor tissue were observed in the G4 group in Fig. 8L compared to the remaining groups. In addition, there was an increase in the proportion of CD8+CD3+ T cells in tumors, spleen, and TDLN in the G4 group compared to the remaining groups (Fig. 8M and fig. S11, A to D). TUNEL staining tumor tissues also showed an

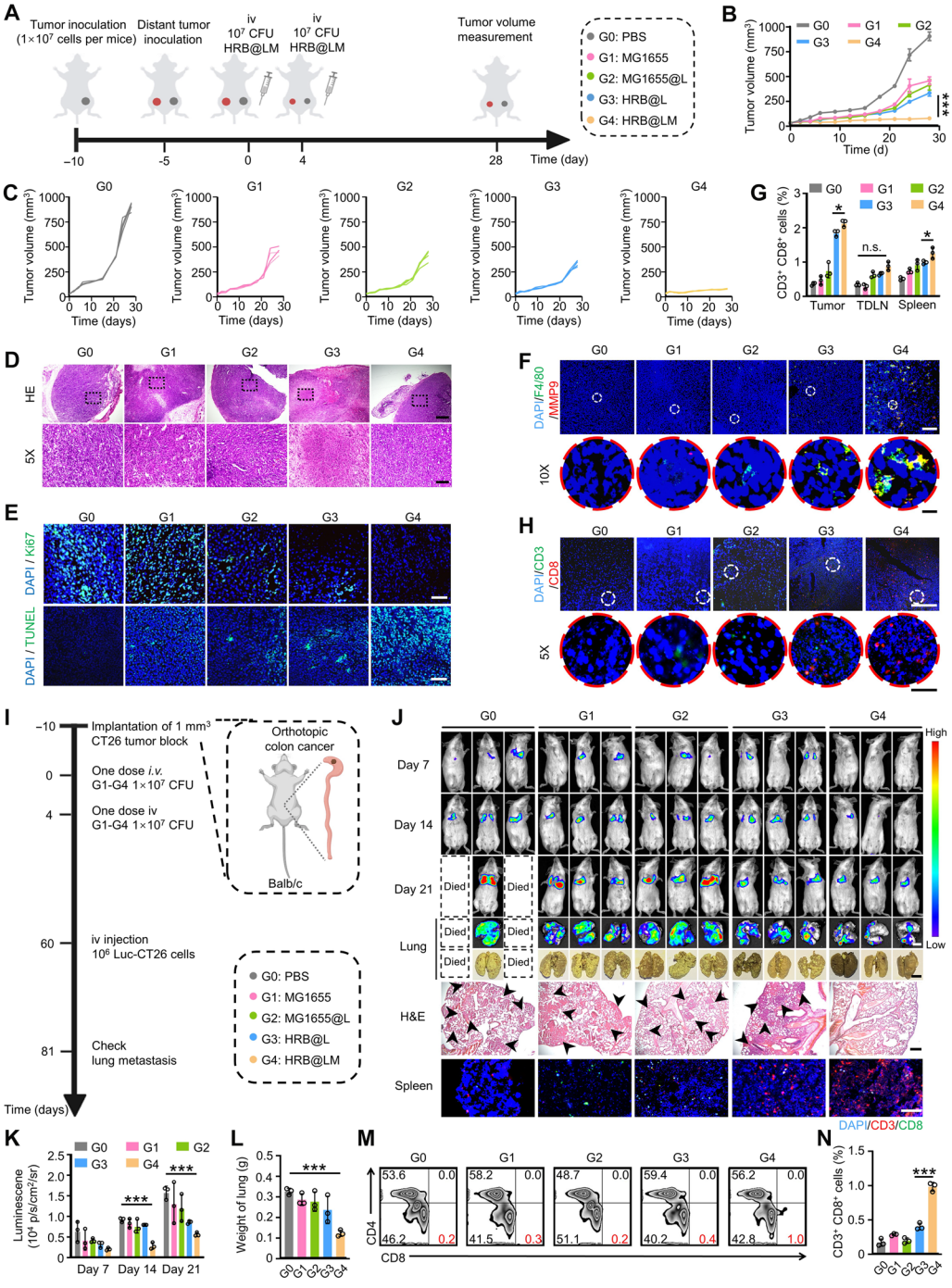

Fig. 7. HRB@LM inhibited distant tumor growth and metastasis. (**A**) Schematic showing the treatment schedule in a distant tumor mouse model. (**B**) Distant tumor growth curve of mice. Data are presented as the means ± SD ($n = 4$). (**C**) Tumor growth curves of individual mouse. (**D**) Representative H&E staining tumor slices. Scale bars, 1 mm and 200 μm (enlarged view). Images were representative of three experiments. (**E**) TUNEL-stained and Ki67-stained tumor slices. Scale bars, 100 μm. Images were representative of three experiments. (**F**) Images of IF staining tumor tissues [green: macrophages, red: M1-like macrophages, and blue: nuclei; scale bars, 100 μm and 10 μm (enlarged view)]. Images were representative of three experiments. (**G**) Quantitative analysis of cytotoxic T cells (CD3+CD8+) in the distant tumor, TDLN, and spleen. Data are presented as the means ± SD ($n = 3$). (**H**) Images of IF staining tumor tissues [green: T cells, red: cytotoxic T cells, and blue: nuclei; scale bars, 100 μm and 20 μm (enlarged view)]. Images were representative of three experiments. (**I**) Schematic illustration of the therapeutic profile of metastatic tumor. (**J**) Representative bioluminescence images (scale bar, 6 mm), Bouin's trichrome fixed lung of mice (scale bar, 6 mm), the representative H&E staining images (scale bar, 500 μm), and representative IF images of CD8+CD3+ T cells (scale bar, 500 μm). Images were representative of three experiments. (**K**) Luminescence of corresponding fluorescence IVIS images in (J). Data are presented as the means ± SD ($n = 3$). (**L**) Weight of the lung ($n = 3$ biologically independent samples). Data are presented as the means ± SD ($n = 3$). (**M** and **N**) Flow cytometry (M) and quantitative analysis (N) of cytotoxic T cells (CD8+CD3+) in the spleen. Data are presented as the means ± SD ($n = 3$). Significance between each of the multiple groups in (B), (G), (K), (L), and (N) was calculated using one-way ANOVA. (A and I) Created with BioRender.

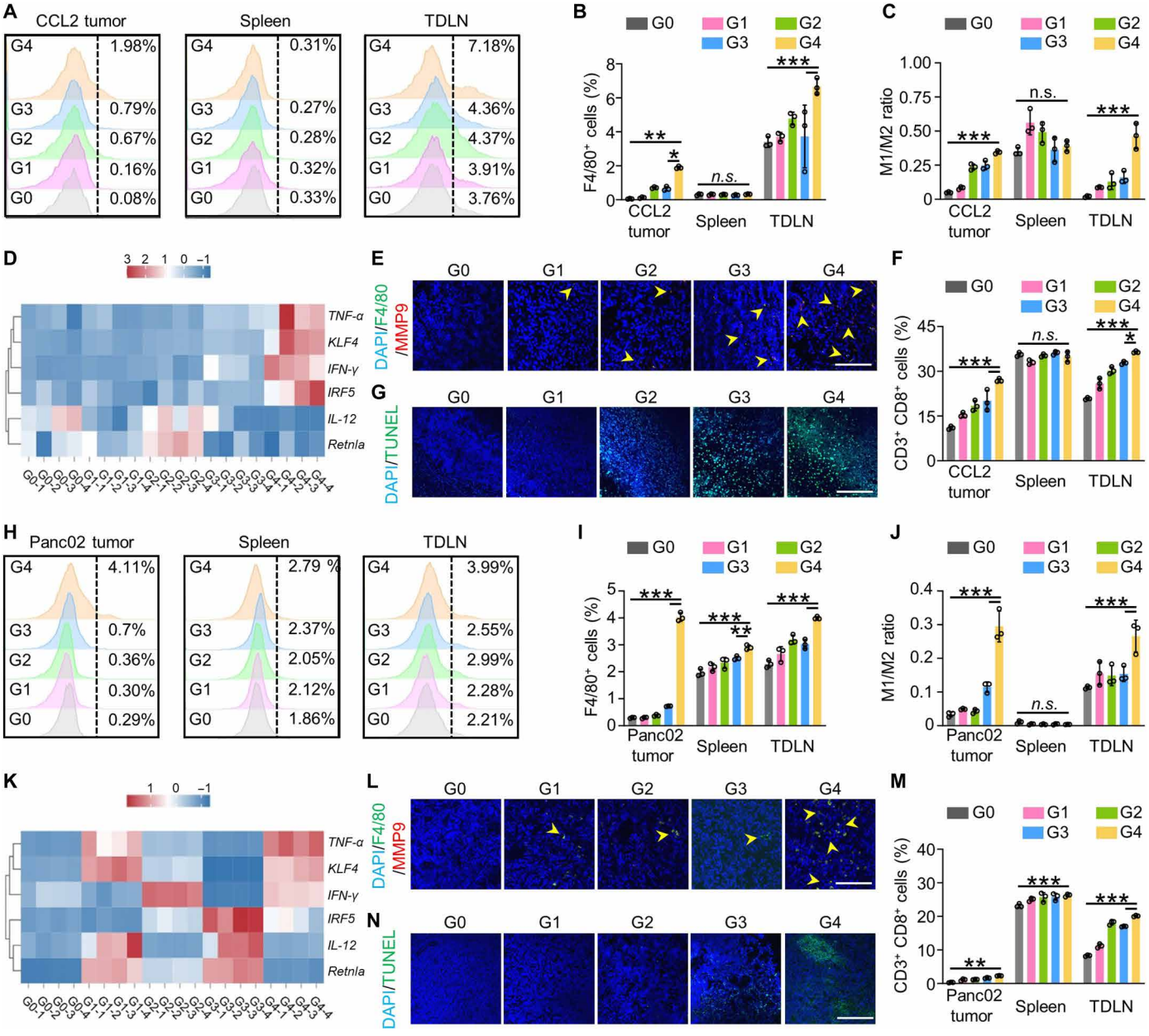

Fig. 8. HRB@LM inhibited lung and pancreatic cancer. (**A** and **B**) Flow cytometry analysis (A) and quantification (B) of the percentage of F4/80+ cells. Data are presented as the means ± SD ($n = 3$). (**C**) Quantification of M1/M2 ratio of CD86+ macrophages (CD86+F4/80+) and CD206+ macrophages (CD206+F4/80+) in the CCL2 tumor, TDLNs, and spleen. Data are presented as the means ± SD ($n = 3$). (**D**) Heatmap of differential gene cluster analysis of M1- and M2-related phenotypes. (**E**) Images of IF staining CCL2 tumor tissues (green: macrophages, red: M1-like macrophages, and blue: nuclei; scale bar, 100 μm). Images were representative of three experiments. (**F**) Flow cytometry quantification of CD8+ T cell (CD8+CD3+) in the CCL2 tumor, TDLN, and spleen. (**G**) TUNEL-stained CCL2 tumor slices. Scale bar, 500 μm. Data are presented as the means ± SD ($n = 3$). (**H** and **I**) Flow cytometry analysis (H) and quantification (I) of the percentage of F4/80+ cells. Data are presented as the means ± SD ($n = 3$). (**J**) Quantification of M1/M2 ratio of CD86+ macrophages (CD86+F4/80+) and CD206+ macrophages (CD206+F4/80+) in the Panc02 tumor, TDLNs, and spleen. Data are presented as the means ± SD ($n = 3$). (**K**) Heatmap of differential gene cluster analysis of M1- and M2-related phenotypes. (**L**) Images of IF staining Panc02 tumor tissues (green: macrophages, red: M1-like macrophages, and blue: nuclei; scale bar, 100 μm). Images were representative of three experiments. (**M**) Flow cytometry quantification of CD8+ T cell (CD8+CD3+) in the Panc02 tumor, TDLN, and spleen. (**N**) TUNEL-stained Panc02 tumor slices. Scale bar, 500 μm. Data are presented as the means ± SD ($n = 3$).

enhancement of green fluorescence signals in the G4 group, which indicated a more significant apoptosis of tumor cells compared to G0, G1, G2, and G3 groups (Fig. 8N). Thus, HRB@LM can also trigger ICT around macrophages in a mouse pancreatic cancer model.

DISCUSSION

We have developed a strategy using nanoliposome-bacteria hybridization system (HRB@LM) as smart Ab "factories" to address the limitations of protein-based ICIs in vivo. The HRB@LM evaded clearance by neutrophils and targeted hypoxic tumor necrotic regions. The loaded bacteria were able to promote the migration of macrophages toward the center of the tumor tissue, but due to the low number of macrophages, it was difficult to infiltrate the tumor effectively. M-CSF specifically released in response to high GSH concentrations recruited and infiltrated large numbers of macrophages that then polarized by LPS into M1 phenotypes. Simultaneously, the expression of plasmid within the Ab factory was promoted under a hypoxic TME, synthesizing aCD47 in situ. Secreted aCD47 directly bind to CD47 receptors on tumor cells, blocking the CD47-SIRPα signaling pathway and enabling precise phagocytosis of tumor cells by macrophages. More antigen presentation of macrophages led to the activation of more CD8+CD3+ T cells, thereby strengthening adaptive immunity against tumors. HRB@LM activated systemic antitumor immune responses and long-term immunity, effectively suppressing primary, distant, and metastatic tumors. Meanwhile, the gut microbiota was restored through modulation of *Lactobacillaceae*, *Streptococcaceae*, and *Gemellaceae* abundance, and mice survival times were significantly extended. Given the excellent tumor-targeting capabilities, TME-triggered synthesis of ICI, antitumor immunity, and regulation of gut microbiota ecology demonstrated by HRB@LM, the reprogramming and redecoration of bacteria as a smart Ab factory represented a highly promising precision medical strategy for future ICT.

MATERIALS AND METHODS

Cell lines and animals

The NIH 3T3 was provided by Wuhan Service Biotechnology Co. Ltd., and the mouse colon cancer cells (CT26, CRL-2638) and RAW 264.7 (TIB-71) were obtained from the American Type Culture Collection (ATCC). The pBV220 plasmid and *E. coli* MG1655 (ATCC 47076) were purchased from Miaoling Bioscience &Technology Co. Ltd. (Wuhan, China). *E. coli* MG1655 was cultured in Luria-Bertani broth medium at 37°C. Also, all cells were cultured in Dulbecco's minimal essential medium [DMEM; 10% (v/v) fetal bovine serum (FBS)] at 37°C in a humidified atmosphere (5% CO_2, 90% humidity), and medium was refreshed every 2 days. Female BALB/c mice weighted 18 to 20 g were purchased from Beijing Vital River Laboratory Animal Technology Co. Ltd. Also, mice were housed in an animal facility under constant environmental conditions (20° to 22°C, 30 to 70% humidity). All animal experiments were approved by the Animal Experiment Ethics Committee of Huazhong University of Science and Technology (Institutional Animal Care and Use Committee number: 4208). Also, the investigators were blinded to group allocation during data collection and analysis.

Hypoxia-induced aCD47 expression

The MG1655 and HRB were divided into four groups incubated under a normoxic and hypoxic environment (37°C), and the photos of bacterial solution were monitored at given time. The supernatant was collected at a given time and mixed with CD47 protein. Also, the concentration of aCD47 can be calculated via a CD47 ELISA kit. The affinity of the released aCD47 to the CD47 protein was also verified by flow cytometry, Western blot (WB), ELISA, and IF staining assay. The outer membrane vesicles (OMVs) of four groups were collected via a bacterial MV isolation kit (Umibio, China). Permeabilization solution (Servicebio, China) was added for 15 min to improve the permeability. CD47-hFc protein was added to the OMVs at room temperature for 30 min, and PBS was added to wash three times. FITC-conjugated goat anti-human IgG (H+L) was then added and cocultured for 30 min. A CytoFLEX flow cytometer was applied to detect the signal after washing three times. IF staining assay was also operated following the above steps and observed via an FV3000 confocal microscope.

HRB@LM construction and characterization

Briefly, DSPE-S-S-mPEG$_{2000}$-NHS (4 mg), lecithin (2 mg), and stearic acid (1 mg) were dissolved in 1 ml of chloroform and lightly stirred. After stirring for 10 min, the precipitate was dried by vacuum pump. One hundred microliters of PBS containing M-CSF (1 μg ml^{-1}) was added and sonicated for 30 min until the solution was clear. Then, 1 ml of *E. coli* MG1655 solution (10^8 CFU ml^{-1}) was added with a 50-μl solution (R0: 0 μl, R1: 0.5 μl, R2: 5 μl, R3: 50 μl, R4: 250 μl, and R5: 500 μl) and stirred gently for 18 hours at 4°C. After centrifugation for three times, the precipitation was suspended with 1 ml of PBS to obtain HRB@LM. The morphology of LM, HRB, and HRB@LM was observed using TEM and scanning electron microscopy. The concentration of M-CSF in LM was determined by a bicinchoninic acid assay (BCA) kit. The encapsulation efficiency (EE) and drug loading (DL) rate in LM was calculated as below

$$\mathrm{EE}\ (\%) = W_A / W_B \times 100\,\%$$

$$\mathrm{DL}\ (\%) = W_A / W_T \times 100\,\%$$

W_A is the total amount of drug in products, W_B is the initial amount of drug used to prepare products, and W_T is the total amount of products.

The in vitro release behavior of LM was carried out in PBS containing 10 μM GSH (pH 6.8) using a dialysis method. Briefly, 500 μl of LM was transferred into dialysis bags (molecular weight cutoff of 4 kDa) with both terminals clamped. The dialysis bags were immediately immersed into 5 ml of PBS solution under magnetic stirring in a water bath (200 rpm, 37°C). Fifty microliters of the medium was withdrawn after 30 min. The withdrawn sample was analyzed by BCA kits and SDS-PAGE electrophoresis. Also, the drug releasing (DR) rate in LM was calculated as below

$$\mathrm{DR}\ (\%) = \left(W_C \times 100\right) / W_A \times 100\,\%$$

W_A is the total amount of drug in products, and W_C is the amount of drug in the withdrawn sample.

To further determine the concentration of M-CSF releasing from HRB@LM, 100 μl of HRB@LM was mixed with 1 ml of PBS containing 10 μM GSH (pH 7.4) for 30 min. After centrifugation at 4000*g* for 10 min, the supernatant was detected via murine M-CSF ELISA kits.

Hypoxic tropism evaluation of HRB@LM

Tropism of HRB@LM toward hypoxic environment was evaluated by using microfluidics (width is 2 cm, and length is 6 cm). The

movement of HRB@LM was recorded by confocal laser scanning microscope (CLSM; Olympus, FV3000). Agarose gel and sodium thiosulfate–contained agarose gel were placed into the two reservoirs of the microfluidic channel. Also, 10^6 CFU of HRB and HRB@LM were dropped in the middle of microfluidic channel. The CLSM image of the region of interest was collected every 15 s. The distance and length of HRB and HRB@LM were calculated, and the chemotactic index (CI) was calculated as the ratio of total displacement to the total migration path.

Penetration evaluation of HRB@LM in a 3D-spheroid tumor model

The 3D tumor spheroids of CT26 cells were established according to the following steps. CT26 cells were maintained under the standard culture conditions. After being treated with 0.25% trypsin, the cells were detached and suspended in DMEM (10% FBS) and the cell density was adjusted to 10^4 cells ml^{-1}. Then, a 200-μl suspension was added into the prime surface 96UZ plate (MS-9096UZ). After centrifugation at 2000*g* for 15 min, the cells were cultured for 2 days, and the cells began to form a 3D-spheroid tumor model. A total of 10^5 CFU of HRB and HRB@LM was added to the medium and cocultured for 2 and 6 hours. The tumor spheroids were washed about three times with PBS and stained with Hoechst 33342 for 15 min. After washing about three times with PBS, the permeability of HRB and HRB@LM into tumor spheroids was studied by CLSM.

Recruitment and polarization of macrophage

A 24-well transwell plate with 8 μm of mean pore size membrane was used to establish the in vitro experimental model. One hundred microliters of PBS, InBac, HRB, and HRB@LM+GSH was added in the lower well. After centrifugation at 2000*g* for 10 min, the RAW264.7 cells (1×10^4 cells per well) were seeded in the upper well with a diameter of 8 μm. After being cocultured for another 12 hours at 37°C, the 24-well plate was then washed three times with PBS and added with 500 μl of 1% (v/v) crystal and 4′,6-diamidino-2-phenylindole (DAPI) for 15 min separately. The images were then recorded, and the absorbance of each well at 590 nm was also tested after adding 100 μl of methanol to dissolve the crystal. The recruited macrophages were also treated with a 70-μm cell filter to prepare single-cell suspensions, and cells were washed with PBS containing 2% FBS. For flow cytometry sorting and analysis, the digested cells were stained with fluorescence-labeled antibodies against protein markers for 30 min. The dilution of antibodies was according to the manufacturer's instructions. After washing with 1640 medium containing 2% FBS, the cells were analyzed on a flow cytometer. Furthermore, the recruited macrophages were stained with Calcein AM and cocultured with DiI-labeled CT26 cells for 24 hours at 37°C. The fluorescence images were then recorded, and the digested cells were analyzed on a flow cytometer.

Twenty microliters of PBS, GSH (10 μM), M-CSF, InBac, HRB@LM, and HRB@LM+GSH (10 μM) was respectively injected into the claws. After 24 hours, the claw tissues were fixed and subjected to H&E staining, followed by differential counting of macrophages and neutrophils. The tissue samples were also analyzed by WB and IF staining.

Recruitment in 3D-spheroid tumor mode

The 3D tumor spheroids of CT26 cells were established according to the above steps. A total of 10^5 CFU HRB and HRB@LM was added to the medium and cocultured for 2 hours. RAW264.7 (10^4 cells) stained with Calcein AM were then added to 3D tumor spheroids and cocultured for 4 and 6 hours. After washing about three times with PBS, the recruitment of RAW264.7 into tumor spheroids of different groups was studied by CLSM.

In vivo treatment of in situ colon cancer

To construct the model of in situ colon cancer, 1×10^6 CT26 cells were injected subcutaneously into the right thigh of Balb/c mice. When the tumor volume reached ~100 mm^3, the mice were anesthetized with 1 to 2% isoflurane in oxygen via a nose cone and the tumors were removed intact. Also, the tumors were divided into 1 mm^3 of tumor blocks. The tumor blocks were sutured to the cecum of the Balb/c mice through a degradable suture, and the whole experiment was aseptically operated. The CT26 tumor-bearing mice were divided into five groups randomly ($n = 5$), including the control group (G0), MG1655 group (G1), MG1655@L group (G2), HRB group (G3), and HRB@LM group (G4). A total of 1×10^7 CFU in 200 μl of saline was injected intravenously into tumor-bearing mice in G1, G2, G3, and G4. The G0 was injected with 200 μl of saline. The treatment procedure was performed day 0 and day 4. Then tumor volumes and mice weights were recorded every 2 days. The calculation formula of tumor volume was volume = (tumor length × tumor width × tumor width)/2. When the mice died, the survival time was recorded. At a preset time, the tumors were collected for H&E staining and IF staining.

Microbial community analyses

CT26 tumor-bearing Balb/c mice were treated as the described earlier; colon tissues were collected on day 14 and stored at −80°C before microbial analysis. Microbiome DNA isolation and 16*S* rRNA gene sequencing were completed by Majorbio Bio-Pharm Technology Co. Ltd. (Shanghai, China).

In vivo inhibition of distant tumor growth and lung metastasis

For the CT26 distant tumor model establishment, 1×10^6 CT26 cells were injected subcutaneously into the right thigh of Balb/c mice. On 5 days after the inoculation, another 1×10^6 CT26 cells were injected into the left thigh of mice. The mice were divided into five groups and treated as described above ($n = 5$) on days 0 and 4 of the first inoculation. Tumor volume and body weight were recorded continuously. The treated mice ($n = 5$) were euthanized on the day 28 by carbon dioxide asphyxiation, and the distant tumor, TDLN, and spleen were collected for flow cytometry analysis of immune cells. TUNEL, H&E, Ki67, F4/80, MMP9, CD3, and CD8 staining were performed on the distant tumor tissues.

For lung metastasis treatment, the treated mice ($n = 5$) were euthanized on day 81 by carbon dioxide asphyxiation and collected their lungs. The weight of lungs was recorded. Also, the lung slices were then stained with H&E to observe the metastasis foci. For flow cytometry analysis of immune cells, the spleens were collected at 67 days after treatments to obtain a single-cell suspension and then analyzed by a flow cytometer as stated above. CD3 and CD8 staining were performed on the spleen.

Statistical analysis

All data were presented as means ± SD. Independent *t* test was used for two groups compared. One-way analysis of variance (ANOVA) using the Tukey post hoc test was used for more than two groups

compared. All statistical analyses were performed by SPSS 26.0. The results were significant when $*P < 0.05$; $**P < 0.01$; $***P < 0.001$; n.s., not significant.

Supplementary Materials

This PDF file includes:

Supplementary Text
Figs. S1 to S11

REFERENCES AND NOTES

1. X. He, C. Xu, Immune checkpoint signaling and cancer immunotherapy. *Cell Res.* **30**, 660–669 (2020).
2. G. Morad, B. A. Helmink, P. Sharma, J. A. Wargo, Hallmarks of response, resistance, and toxicity to immune checkpoint blockade. *Cell* **184**, 5309–5337 (2021).
3. P. Sharma, S. Goswami, D. Raychaudhuri, B. A. Siddiqui, P. Singh, A. Nagarajan, J. Liu, S. K. Subudhi, C. Poon, K. L. Gant, S. M. Herbrich, S. Anandhan, S. Islam, M. Amit, G. Anandappa, J. P. Allison, Immune checkpoint therapy-current perspectives and future directions. *Cell* **186**, 1652–1669 (2023).
4. J. Pan, X. Li, B. Shao, F. Xu, X. Huang, X. Guo, S. Zhou, Self-blockade of PD-L1 with bacteria-derived outer-membrane vesicle for enhanced cancer immunotherapy. *Adv. Mater.* **34**, 2106307 (2022).
5. Q. Sun, Z. Hong, C. Zhang, L. Wang, Z. Han, D. Ma, Immune checkpoint therapy for solid tumors: Clinical dilemmas and future trends. *Signal Transduct. Target. Ther.* **8**, 320 (2023).
6. A. Mantovani, P. Allavena, F. Marchesi, C. Garlanda, Macrophages as tools and targets in cancer therapy. *Nat. Rev. Drug Discov.* **21**, 799–820 (2022).
7. Z. Tang, M. C. Zhong, J. Qian, C. C. Galindo, D. Davidson, J. Li, Y. Zhao, E. Hui, A. Veillette, CD47 masks pro-phagocytic ligands in cis on tumor cells to suppress antitumor immunity. *Nat. Immunol.* **24**, 2032–2041 (2023).
8. Y. Guo, Q. Bao, P. Hu, J. Shi, Nanomedicine-based co-delivery of a calcium channel inhibitor and a small molecule targeting CD47 for lung cancer immunotherapy. *Nat. Commun.* **14**, 7306 (2023).
9. D. Candas-Green, B. Xie, J. Huang, M. Fan, A. Wang, C. Menaa, Y. Zhang, L. Zhang, D. Jing, S. Azghadi, W. Zhou, L. Liu, N. Jiang, T. Li, T. Gao, C. Sweeney, R. Shen, T. Y. Lin, C. X. Pan, O. M. Ozpiskin, G. Woloschak, D. J. Grdina, A. T. Vaughan, J. M. Wang, S. Xia, A. M. Monjazeb, W. J. Murphy, L. Q. Sun, H. W. Chen, K. S. Lam, R. R. Weichselbaum, J. J. Li, Dual blockade of CD47 and HER2 eliminates radioresistant breast cancer cells. *Nat. Commun.* **11**, 4591 (2020).
10. Z. Wang, B. Li, S. Li, W. Lin, Z. Wang, S. Wang, W. Chen, W. Shi, T. Chen, H. Zhou, E. Yinwang, W. Zhang, H. Mou, X. Chai, J. Zhang, Z. Lu, Z. Ye, Metabolic control of CD47 expression through LAT2-mediated amino acid uptake promotes tumor immune evasion. *Nat. Commun.* **13**, 6308 (2022).
11. J. T. Sockolosky, M. Dougan, J. R. Ingram, C. C. M. Ho, M. J. Kauke, S. C. Almo, H. L. Ploegh, K. C. Garcia, Durable antitumor responses to CD47 blockade require adaptive immune stimulation. *Proc. Natl. Acad. Sci. U.S.A.* **113**, E2646–E2654 (2016).
12. J.-X. Fan, X.-H. Liu, X.-N. Wang, M.-T. Niu, Q.-W. Chen, D.-W. Zheng, J.-S. Wei, X.-Q. Yang, X. Zeng, X.-Z. Zhang, Antibody engineered platelets attracted by bacteria-induced tumor-specific blood coagulation for checkpoint inhibitor immunotherapy. *Adv. Funct. Mater.* **31**, 2009744 (2021).
13. C. R. Gurbatri, N. Arpaia, T. Danino, Engineering bacteria as interactive cancer therapies. *Science* **378**, 858–864 (2022).
14. L. Zhai, L. Fu, W. Wei, D. Zheng, Advances of bacterial biomaterials for disease therapy. *ACS Synth. Biol.* **13**, 1400–1411 (2024).
15. W. Song, A. C. Anselmo, L. Huang, Nanotechnology intervention of the microbiome for cancer therapy. *Nat. Nanotechnol.* **14**, 1093–1103 (2019).
16. C. R. Gurbatri, G. A. Radford, L. Vrbanac, J. Im, E. M. Thomas, C. Coker, S. R. Taylor, Y. Jang, A. Sivan, K. Rhee, A. A. Saleh, T. Chien, F. Zandkarimi, I. Lia, T. R. M. Lannagan, T. Wang, J. A. Wright, H. Kobayashi, J. Q. Ng, M. Lawrence, T. Sammour, M. Thomas, M. Lewis, L. Papanicolas, J. Perry, T. Fitzsimmons, P. Kaazan, A. Lim, A. M. Stavropoulos, D. A. Gouskos, J. Marker, C. Ostroff, G. Roger, N. Arpaia, D. L. Worthley, S. L. Woods, T. Danino, Engineering tumor-colonizing *E. coli* Nissle 1917 for detection and treatment of colorectal neoplasia. *Nat. Commun.* **15**, 646 (2024).
17. W. Chen, Y. Wang, M. Qin, X. Zhang, Z. Zhang, X. Sun, Z. Gu, Bacteria-driven hypoxia targeting for combined biotherapy and photothermal therapy. *ACS Nano* **12**, 5995–6005 (2018).
18. X. Yi, H. Zhou, Y. Chao, S. Xiong, J. Zhong, Z. Chai, K. Yang, Z. Liu, Bacteria-triggered tumor-specific thrombosis to enable potent photothermal immunotherapy of cancer. *Sci. Adv.* **6**, 1–13 (2020).
19. J. X. Fan, M. T. Niu, Y. T. Qin, Y. X. Sun, X. Z. Zhang, Progress of engineered bacteria for tumor therapy. *Adv. Drug Deliv. Rev.* **185**, 114296 (2022).
20. S. Chowdhury, S. Castro, C. Coker, T. E. Hinchliffe, N. Arpaia, T. Danino, Programmable bacteria induce durable tumor regression and systemic antitumor immunity. *Nat. Med.* **25**, 1057–1063 (2019).
21. S. Zhou, Bacteria synchronized for drug delivery. *Nature* **536**, 33–34 (2016).
22. Y. Chen, M. Du, Z. Yuan, Z. Chen, F. Yan, Spatiotemporal control of engineered bacteria to express interferon-γ by focused ultrasound for tumor immunotherapy. *Nat. Commun.* **13**, 4468 (2022).
23. Z. Li, Y. Wang, J. Liu, P. Rawding, J. Bu, S. Hong, Q. Hu, Chemically and biologically engineered bacteria-based delivery systems for emerging diagnosis and advanced therapy. *Adv. Mater.* **33**, e2102580 (2021).
24. X. Ke, H. Xiao, Y. Peng, X. Xia, X. Wang, Nitrogen deficiency modulates carbon allocation to promote nodule nitrogen fixation capacity in soybean. *Exp. Dermatol.* **4**, 20230104 (2024).
25. Y. Li, X. L. Lei, X. S. Zhang, B. Zhang, Y. G. Hu, M. Guan, K. Cheng, W. Chen, B. Liu, J. X. Fan, Y. D. Zhao, Self-initiated nano-micelles mediated covalent modification of mRNA for labeling and treatment of tumors. *Angew. Chem. Int. Ed. Engl.* **63**, e202411598 (2024).
26. Z. Cao, X. Wang, Y. Pang, S. Cheng, J. Liu, Biointerfacial self-assembly generates lipid membrane coated bacteria for enhanced oral delivery and treatment. *Nat. Commun.* **10**, 5783 (2019).
27. J. X. Fan, M. Y. Peng, H. Wang, H. R. Zheng, Z. L. Li, C. X. Li, X. N. Wang, X. H. Liu, S. X. Cheng, X. Z. Zhang, Engineered bacterial bioreactor for tumor therapy *via* Fenton-like reaction with localized H_2O_2 generation. *Adv. Mater.* **31**, 1808278 (2019).
28. O. Felfoul, M. Mohammadi, S. Taherkhani, D. Lanauze, Y. Z. Xu, D. Loghin, S. Essa, S. Jancik, D. Houle, M. Lafleur, L. Gaboury, M. Tabrizian, N. Kaou, M. Atkin, T. Vuon, G. Batist, N. Beauchemin, D. Radzioch, S. Martel, Magneto-aerotactic bacteria deliver drug-containing nanoliposomes to tumor hypoxic regions. *Nat. Nanotechnol.* **11**, 941–947 (2016).
29. Z. Luo, M. Tian, G. Yang, Q. Tan, Y. Chen, G. Li, Q. Zhang, Y. Li, P. Wan, J. Wu, Hypoxia signaling in human health and diseases: Implications and prospects for therapeutics. *Signal Transduct. Target. Ther.* **7**, 218 (2022).
30. S. Liu, R. Guo, H. Xu, J. Yang, H. Luo, S. J. Yeung, K. Li, M. H. Lee, R. Yang, 14-3-3σ-NEDD4L axis promotes ubiquitination and degradation of HIF-1α in colorectal cancer. *Cell Rep.* **42**, 112870 (2023).
31. I. Godet, Y. J. Shin, J. A. Ju, I. C. Ye, G. Wang, D. M. Gilkes, Fate-mapping post-hypoxic tumor cells reveals a ROS-resistant phenotype that promotes metastasis. *Nat. Commun.* **10**, 4862 (2019).
32. J. Shao, M. Xuan, H. Zhang, X. Lin, Z. Wu, Q. He, Chemotaxis-guided hybrid neutrophil micromotors for targeted drug transport. *Angew. Chem. Int. Ed. Engl.* **56**, 12935–12939 (2017).
33. M. Guan, K. Cheng, X. Xie, Y. Li, M. Ma, B. Zhang, S. Chen, W. Chen, B. Liu, J. X. Fan, Y. D. Zhao, Regulating copper homeostasis of tumor cells to promote cuproptosis for enhancing breast cancer immunotherapy. *Nat. Commun.* **15**, 10060 (2024).
34. Q. W. Chen, J. W. Wang, X. N. Wang, J. X. Fan, X. H. Liu, B. Li, Z. Y. Han, S. X. Cheng, X. Z. Zhang, Inhibition of tumor progression through the coupling of bacterial respiration with tumor metabolism. *Angew. Chem. Int. Ed. Engl.* **59**, 21562–21570 (2020).
35. H. R. Jia, Y. X. Zhu, Y. Liu, Y. Guo, S. M. Sayed, X. Y. Zhu, X. Cheng, F. G. Wu, Direct chemical editing of Gram-positive bacterial cell walls *via* an enzyme-catalyzed oxidative coupling reaction. *Exp. Dermatol.* **2**, 20220010 (2022).
36. Q. Li, H. Chan, W. X. Liu, C. A. Liu, Y. Zhou, D. Huang, X. Wang, X. Li, C. Xie, W. Y. Liu, X. S. Wang, S. K. Ng, H. Gou, L. Y. Zhao, W. Fong, L. Jiang, Y. Lin, G. Zhao, F. Bai, X. Liu, H. Chen, L. Zhang, S. H. Wong, M. T. V. Chan, W. K. K. Wu, J. Yu, *Carnobacterium maltaromaticum* boosts intestinal vitamin D production to suppress colorectal cancer in female mice. *Cancer Cell* **41**, 1450–1465.e8 (2023).
37. H. Wu, D. Zhong, Z. Zhang, Y. Wu, Y. Li, H. Mao, K. Luo, D. Kong, Q. Gong, Z. Gu, A bacteria-inspired morphology genetic biomedical material: Self-propelled artificial microbots for metastatic triple negative breast cancer treatment. *ACS Nano* **15**, 4845–4860 (2021).
38. X. Liu, Y. Pu, K. Cron, L. Deng, J. Kline, W. A. Frazier, H. Xu, H. Peng, Y. X. Fu, M. M. Xu, CD47 blockade triggers T cell-mediated destruction of immunogenic tumors. *Nat. Med.* **21**, 1209–1215 (2015).
39. J. L. Liang, X. K. Jin, G. F. Luo, S. M. Zhang, Q. X. Huang, Y. T. Lin, X. C. Deng, J. W. Wang, W. H. Chen, X. Z. Zhang, Immunostimulant hydrogel-guided tumor microenvironment reprogramming to efficiently potentiate macrophage-mediated cellular phagocytosis for systemic cancer immunotherapy. *ACS Nano* **17**, 17217–17232 (2023).
40. C. A. Lozupone, J. I. Stombaugh, J. I. Gordon, J. K. Jansson, R. Knight, Diversity, stability and resilience of the human gut microbiota. *Nature* **489**, 220–230 (2012).
41. D. W. Zheng, W. W. Deng, W. F. Song, C. C. Wu, J. Liu, S. Hong, Z. N. Zhuang, H. Cheng, Z. J. Sun, X. Z. Zhang, Biomaterial-mediated modulation of oral microbiota synergizes with PD-1 blockade in mice with oral squamous cell carcinoma. *Nat. Biomed. Eng.* **6**, 32–43 (2022).
42. D. W. Zheng, P. Pan, K. W. Chen, J. X. Fan, C. X. Li, H. Cheng, X. Z. Zhang, An orally delivered microbial cocktail for the removal of nitrogenous metabolic waste in animal models of kidney failure. *Nat. Biomed. Eng.* **4**, 853–862 (2020).

43. Q. Zhang, Q. Zhao, T. Li, L. Lu, F. Wang, H. Zhang, Z. Liu, H. Ma, Q. Zhu, J. Wang, X. Zhang, Y. Pei, Q. Liu, Y. Xu, J. Qie, X. Luan, Z. Hu, X. Liu, *Lactobacillus* plantarum-derived indole-3-lactic acid ameliorates colorectal tumorigenesis *via* epigenetic regulation of CD8+ T cell immunity. *Cell Metab.* **35**, 943–960 (2023).
44. N. S. Oh, J. Y. Lee, Y.-T. Kim, S. H. Kim, J.-H. Lee, Cancer-protective effect of a synbiotic combination between *Lactobacillus gasseri* 505 and a *Cudrania tricuspidata* leaf extract on colitis-associated colorectal cancer. *Gut Microbes.* **12**, 1785803 (2020).
45. J. Corredoira-Sánchez, F. García-Garrote, R. Rabuñal, L. López-Roses, M. J. García-País, E. Castro, R. González-Soler, A. Coira, J. Pita, M. J. López-Álvarez, M. P. Alonso, J. Varela, Association between bacteremia due to *Streptococcus gallolyticus subsp. gallolyticus* (*Streptococcus bovis I*) and colorectal neoplasia: A case-control study. *Clin. Infect. Dis.* **55**, 491–496 (2012).
46. A. Boleij, M. M. H. J. van Gelder, D. W. Swinkels, H. Tjalsma, Clinical importance of *Streptococcus gallolyticus* infection among colorectal cancer patients: Systematic review and meta-analysis. *Clin. Infect. Dis.* **53**, 870–878 (2011).
47. H. Chen, T. Tong, S. Y. Lu, L. Ji, B. Xuan, G. Zhao, Y. Yan, L. Song, L. Zhao, Y. Xie, X. Leng, X. Zhang, Y. Cui, X. Chen, H. Xiong, T. Yu, X. Li, T. Sun, Z. Wang, J. Chen, Y. X. Chen, J. Hong, J. Y. Fang, Urea cycle activation triggered by host-microbiota maladaptation driving colorectal tumorigenesis. *Cell Metab.* **35**, 651–666.e7 (2023).

Acknowledgments: We thank the Analytical and Testing Center (HUST), the Research Core Facilities for Life Science (HUST) for the help of measurement. We thank the support from the Key Laboratory of Biomedical Polymers of Ministry of Education, Wuhan University, for the assistance. We also thank the Elabscience Biotechnology Co. Ltd. for assisting in cytokine detection. Figures 1A, 2 (A and O), 3I, 4 (A and K), 5A, and 7 (A and I) were created with BioRender.com released under a Creative Commons Attribution 4.0 International license (https://creativecommons.org/licenses/by/4.0/). **Funding:** This work was supported by the National Natural Science Foundation of China (grant nos. 52103319 to J.-X.F., 62375093 to Y.-D.Z., 62305121 to K.C., and 82373104 to B.L.), the China Postdoctoral Science Foundation Funded Project (grant no. 2023T160247 to K.C.), the Technology Innovation Program of Hubei Province (grant no. 2024BCB058 to Y.-D.Z.), and the Natural Science Foundation of Hubei Province of China (grant no. 2024AFB700 to S.C.). **Author contributions:** Conceptualization: X.-T.X., M.G., and J.-X.F. Methodology: X.-T.X., Y.L., B.Z., and P.-S.D. Investigation: X.-T.X., M.G., K.C., Y.-T.Z., and L.-F.T. Visualization: X.-T.X., M.G., and J.-X.F. Funding acquisition: S.C., J.-X.F., Y.-D.Z., and B.L. Supervision: X.-T.X., S.C., J.-X.F., Y.-D.Z., and B.L. Project administration: S.C., J.-X.F., Y.-D.Z., and B.L. Writing—original draft: X.-T.X., M.G., K.C., and J.-X.F. Writing—review and editing: X.-T.X., S.C., J.-X.F., Y.-D.Z., and B.L. **Competing interests:** The authors declare that they have no competing interests. **Data and materials availability:** Sequencing data are available on NCBI reference sequence: NZ_LR881938. All data needed to evaluate the conclusions in the paper are present in the paper and/or the Supplementary Materials. Source data are provided as a Source Data file (https://figshare.com/s/c53777f585f188869551).

Submitted 9 October 2024
Accepted 25 February 2025
Published 26 March 2025
10.1126/sciadv.adt7298